Materials Advances

ROYAL SOCIETY OF CHEMISTRY

PAPER

View Article Online
View Journal | View Issue

Cite this: *Mater. Adv.*, 2024, 5, 7789

Cabazitaxel-loaded redox-responsive nanocarrier based on D-alpha-tocopheryl-chitosan and hyaluronic acid for improved anti-tumor efficacy in DMBA-induced breast cancer model†

Abhishek Jha, [a] Manish Kumar, [a] Pooja Goswami, [b] Kanchan Bharti, [a] Manjit Manjit, [a] Ashutosh Gupta, [c] Sudheer Moorkoth, [c] Biplob Koch *[b] and Brahmeshwar Mishra *[a]

Received 30th May 2024,
Accepted 2nd September 2024

DOI: 10.1039/d4ma00556b

rsc.li/materials-advances

The study involved the formulation of cabazitaxel loaded D-alpha-tocopheryl succinate/chitosan conjugate (CSVE) and hyaluronic acid (HA) based redox-responsive nanoparticles crosslinked using 3,3′-dithiodipropionic acid (DTPA). The nanoparticle surface was functionalized with cetuximab (Cmab) to give CSVE/HA/DTPA/Cmab NP for EGFR targeted delivery of the payload. The formulations were subjected to particle analysis, morphological assessment, solid-state characterization, and *in vitro* drug release studies. The results showed cationic, sub-200 nm sized spherical particles with the glutathione-responsive release of cabazitaxel. *In vitro* studies revealed a marked decrease in the IC_{50} value, improved cellular uptake, and a superior apoptotic effect. To determine the *in vivo* efficacy of the formulation, pharmacokinetic assessment, tumor regression analysis, and survival analysis were performed. The nanoparticles showed improved pharmacokinetic and anti-tumor efficacy compared to free cabazitaxel. The prepared nanoparticles demonstrated immense potential in targeted delivery of the payload for enhanced breast cancer therapy.

1. Introduction

Breast cancer is the most prevalent type of cancer accounting for over 25 percent of total cancer cases worldwide. According to GLOBOCAN 2020, there were an estimated 2.3 million new cases of breast cancer globally in 2020 with approximately 685 000 deaths in the same year. The age-standardized mortality rate for breast cancer was reported to be 13.0 per 100 000 women and an estimated 5-year prevalence of breast cancer (both sexes, all ages) of around 7.8 million cases.[1] This makes breast cancer a significant health concern and underscores the importance of ongoing efforts in the research to understand its prevalence and the development of effective treatment strategies. Radiation therapy and chemotherapy are the traditional therapeutic strategies in case the surgical removal is not feasible. However, poor clinical results, toxic effects, and drug resistance are the major limitations of traditional treatment strategies.

Nanoparticles have shown great promise in ameliorating the limitations associated with traditional treatment strategies for breast cancer.[2,3] They can utilize the EPR effect to enter the tumor cells.[4] Their submicron size improves cellular uptake and facilitates intracellular delivery of therapeutic agents.[5,6] To improve their selectivity, the surface of nanoparticles can be functionalized with specific ligands,[7,8] to ensure precise intracellular delivery of therapeutics *via* receptor mediated endocytosis.[9,10] To further improve the precise delivery of therapeutics at the target site, nanoparticles responsive to physiological stimuli can be designed.[11–14] Recently, redox responsive nanosystems have gained enormous attention. They release their payload selectively in the presence of elevated levels of reducing agents like glutathione (GSH) in cancer cells which triggers the disassembly of nanoparticles.[11,15,16] This selectivity prevents the premature drug release in blood circulation, minimizes off-target toxicity and ensures a higher

[a] *Department of Pharmaceutical Engineering & Technology, Indian Institute of Technology (BHU), Varanasi - 221005, Uttar Pradesh, India. E-mail: bmishra.phe@iitbhu.ac.in, abhishekjha.phe17@itbhu.ac.in, manishkumar.rs.phe19@itbhu.ac.in, kanchan.bharti.rs.phe18@itbhu.ac.in, manjit.rs.phe20@itbhu.ac.in*

[b] *Genotoxicology and Cancer Biology Laboratory, Department of Zoology Institute of Science, Banaras Hindu University, Varanasi - 221005, Uttar Pradesh, India. E-mail: biplob@bhu.ac.in, pooja1428@bhu.ac.in*

[c] *Department of Pharmaceutical Quality Assurance, Manipal College of Pharmaceutical Sciences, Manipal Academy of Higher Education, Manipal - 576104, Karnataka, India. E-mail: ashutoshgupta086@gmail.com, moorkoth.s@manipal.edu*

† Electronic supplementary information (ESI) available. See DOI: https://doi.org/10.1039/d4ma00556b

concentration of the drug at the target site. Redox-responsive nanoparticles can also address multidrug resistance by facilitating intracellular accumulation of the drug payload, thereby enhancing the efficacy of cancer treatments.

Natural polysaccharides as biomaterials have shown immense potential in the development of nanosized drug delivery platforms[17] owing to their biocompatibility, biodegradability, and non-toxicity.[18,19] Polysaccharides such as chitosan and their derivatives have been extensively explored for the development of nanomedicine responsive to tumor microenvironments.[20–22] Chitosan, a cationic biopolymer derived from chitin, when used in the fabrication of nanoparticles, interacts with negatively charged cell membranes and enhances their cellular internalization.[23,24] Chitosan can also be modified to achieve specific properties for drug delivery applications.[12,25] Conjugating a hydrophobic moiety like D-alpha-tocopherol (vitamin E) on the hydrophilic chitosan backbone may make the conjugate amphiphilic for improving the loading of poorly aqueous soluble drugs.[26–28] Vitamin E also modulates the signaling pathways such as the PI3K/AKT/mTOR pathway involved in cancer progression and drug resistance.[29] Besides, the ability of vitamin E to neutralize reactive oxygen species (ROS) that promotes drug resistance in cancer cells also contributes to overcoming drug resistance by modulating the tumor microenvironment.[30–33] Another amphiphilic derivative of vitamin E is D-alpha-tocopheryl polyethylene glycol 1000 succinate (TPGS) which provides steric stabilization to nanoparticles, prevents aggregation, and enhances cellular uptake.[34,35] It forms a hydration layer around the nanoparticles, reducing particle–particle interactions, and provides stealth against immune recognition, thereby prolonging their circulation in bloodstream.[36] TPGS also provides a reactive terminal functional group for ligand conjugation on the surface of nanomedicine.[35] Moreover, CSVE and TPGS together can form a mixed micellar structure due to a common hydrophobic core (vitamin E) that provides a better hydrophobic microenvironment for encapsulation and stabilization of hydrophobic drugs in their core.[26,34] CSVE/TPGS-based mixed micelles can also be combined with other polysaccharides like hyaluronic acid to create a hybrid nanostructure with improved performance.[37] Hyaluronic acid (HA), an anionic polysaccharide, can enhance the stability of CSVE/TPGS-based micelles as a carrier.[38,39] The positive and negative charges of chitosan and hyaluronic acid interact to form a complex that enhances self-assembly into nanoparticles through ionic gelation.[40] Hyaluronic acid (HA) also has the ability to interact with CD44 receptors, which are overexpressed on cancer cell surfaces.[13,38,39] Thus, incorporation of HA into nanocarriers can provide targeted drug delivery to the tumor.[13,41] HA also enhances the penetration of nanoparticles into tumor tissue, ensuring better distribution of therapeutic payload in the complex tumor microenvironment. Furthermore, crosslinking of these hybrid structures can be achieved using a crosslinker like 3,3′-dithiodipropionic acid (DTPA, a redox-responsive linker)[42,43] that utilizes the free amine group of the CSVE structure to form a stable and compact nanostructure with redox-responsive characteristics.

In the present study, cabazitaxel, an FDA-approved antineoplastic agent, was used as the model hydrophobic drug.[44] It disrupts microtubule dynamics in cancer cells, inhibiting mitosis and causing apoptosis.[45] Currently approved for metastatic castration-resistant prostate cancer, it is used in patients who have previously received docetaxel-based chemotherapy.[46,47] However, studies are ongoing to explore its use in other cancer types and its potential in combination with other therapeutic agents.[48] Also, cabazitaxel belonging to BCS Class IV drugs exhibits limited aqueous solubility and poor permeability.[49] In addition, associated toxicity to major organs due to non-selective distribution other than the tumor site is another major challenge. Thus, strategies to improve the properties of cabazitaxel for smoothening the delivery is required which can be attained by formulating their nanoparticles. The use of nanoparticles may address the above issues and ensure higher therapeutic response by minimizing off-target distribution, prolonging systemic circulation, controlling drug release and facilitating accumulation at the tumor site.[49,50] The nanoparticles can be modified with a stimuli responsive and targeting moiety to further specify their delivery to the tumor microenvironment and cancer cells, thereby reducing off-target distribution and drug-associated adverse effects.[51–53] The current study involves the synthesis of vitamin-E conjugated chitosan (CSVE). The synthesized CSVE and HA were used for the development of TPGS-COOH stabilized sub-200 nm sized self-assembled hybrid nanoparticles. The prepared particles were further crosslinked with DTPA to endow redox-responsive characteristics. The particles were subsequently functionalized by conjugating cetuximab on their surface to further improve the selectivity of the nanoparticles toward cancer cells (details in Fig. S1, ESI†).

2. Materials and methods

2.1. Materials

D-Alpha-tocopheryl polyethylene glycol 1000 succinate (TPGS) was obtained as a gift sample from Antares Health Products, St. Charles, USA. Cabazitaxel was a gift sample from Hetero Labs, India. Sodium hyaluronate (HA) with an average molecular weight of ~9.4 kDa was provided as a gift sample by Shandong Topscience Biotech Co. Ltd, Shandong, PRC. All the other chemicals and solvents used in the experiments were of high purity.

The MDA-MB-231, T47D, and HCT116 cell lines were procured from NCCS Pune, India. DMEM (Dulbecco's Modified Eagle Medium) and 12-well and 6-well cell culture plates were procured from Genetix (Genetics Biotech Asia Pvt. Ltd). 96-well plates and T-25 flasks were obtained from Eppendorf. Penicillin–streptomycin, Trypsin-EDTA and FBS (fetal bovine serum) were purchased from Gibco.

2.2. Formulation of CSVE-based nanoparticles

The hybrid CSVE/HA nanoparticles (CSVE/HA-NP) were prepared using the solvent emulsification–evaporation method. Briefly, the CSVE conjugate (detailed in the ESI†) and TPGS were dissolved in 10 ml of distilled water and kept under

stirring. CBT (5 mg ml^{-1}) in chloroform was added to the CSVE/TPGS solution and probe-sonicated using a 6 mm probe at 70% amplitude for 7 minutes in an ice-bath.[28] The solution was kept under stirring at 200 rpm for 3 h for the organic solvent to evaporate. The anionic TPGS and cationic CSVE form a stable micellar assembly due to their amphiphilic nature and common hydrophobic group. Subsequently, 5 ml of HA solution in distilled water (2 mg ml^{-1}) was added dropwise and stirred for 2 h.[54]

To prepare redox-responsive nanoparticles (CSVE/HA/DTPA NP), only 2.5 ml of HA (2 mg ml^{-1}) was used, while DTPA was used as the crosslinker according to a previously reported method with minor modifications.[14,55] For this, 72 mg of sulfo-NHS and 64 mg of EDC were dissolved in 2.5 ml of water then 12 mg of DTPA was added and stirred for 30 min. This solution was added dropwise into the CSVE/HA nanoparticle suspension and stirred for 3 h. For the preparation of targeted nanoparticles (CSVE/HA/DTPA/Cmab), CSVE/HA/DTPA was incubated with NHS and EDC for 30 minutes followed by the addition of cetuximab (2.5 mg) and stirred for 3 h.[56] The nanoparticles were washed thrice with distilled water using Amicon® Ultra centrifugal filters (MWCO 30 kDa). The washed nanoparticles were then subjected to lyophilization and stored at 4–8 °C until further use. In preparing coumarin-6 (CM6) loaded nanoparticles, 0.3 mg of CM6 was added instead of cabazitaxel to 1 ml of chloroform mentioned above. Also, for preparing chitosan-based hybrid nanoparticles, CSVE was replaced with water soluble CSO.

2.3. Characterization of CSVE-based nanoparticles

2.3.1. Assessment of hydrodynamic particle size, zeta potential, and particle morphology. The size and zeta potential (ζ) were determined using a Malvern Zetasizer (Nano ZS90, Malvern Instruments). The morphology of the nanoparticles was evaluated using a Tecnai G2 20 TWIN transmission electron microscope (TEM; FEI, USA), a Nova Nano SEM 450 scanning electron microscope (SEM; FEI, USA), and an NTEGRA Prima scanning probe microscope (SPM/AFM; NT-MDT Service & Logistics Ltd).

2.3.2. Estimation of encapsulation efficiency. The encapsulation efficiency of the nanoparticles was calculated using the analytical method. Briefly, 10 mg of nanoparticles were added into 2 ml of ACN and bath-sonicated for 30 minutes. The solution was then filtered using a 0.1 μm pore-size syringe filter. The filtered solution was then analyzed using HPLC to estimate the amount of encapsulated drug. The percentage of drug loading was also calculated using the data from the calculation of the amount of encapsulated drug.

2.3.3. Solid-state characterization (XRD, FTIR, DSC, and XPS). Fourier-transform infrared (FT-IR) spectra of the pure drug (CBT), CSVE, HA, TPGS (TPGS-COOH) and all the formulations were acquired using a JASCO FT/IR-4200 type A (JASCO Co., Tokyo, Japan) using the KBr method. Differential scanning calorimetry (DSC) was performed using a DSC-60 Plus (Shimadzu, Asia Pacific). X-ray diffraction (XRD) analysis of lyophilized samples was performed using a Rigaku Miniflex 600 Desktop X-ray Diffraction System (RIGAKU Corporation). X-ray photoelectron spectroscopy (XPS) was used to assess the surface chemistry of the formulations using a K-Alpha (Thermo Fisher Scientific).

2.4. Drug release studies

Drug release studies were performed using the dialysis method.[57] Herein, the nanoparticle suspensions equivalent to 5 mg of cabazitaxel were loaded in a sealed pouch of dialysis membrane (Spectra/Por® 7, 1000 Da MWCO) and immersed in 50 ml of the medium. 1 ml of the medium was collected at predetermined time intervals. The samples were then filtered with 0.1 μm pore size membrane filters and analyzed using the HPLC-based analytical method. The drug release was investigated in phosphate buffered saline (pH 7.4), acetate buffer (pH 5.5), and acetate buffer (pH 5.5)/GSH (10 mM).

2.5. Stability of lyophilized nanoparticles

To assess the stability of the prepared formulations, washed and purified CSVE/HA/DTPA NP and CSVE/HA/DTPA/Cmab NP were lyophilized and packed in airtight borosilicate glass vials and kept in a refrigerator at 4 °C for predetermined intervals. After day 7, 15, 30, 90, and 180, the lyophilized formulation was resuspended in deionized water and assessed for hydrodynamic particle size, zeta potential, PDI, and entrapment efficiency.

2.6. *In vitro* cell line studies

2.6.1. Cell line maintenance. The MDA-MB-231, T47D, and HCT116 cells were incubated in a humidified CO_2 incubator at 37 °C while being cultured in DMEM with FBS and penicillin–streptomycin solution.

2.6.2. Cytotoxicity assay. The cytotoxicity of the prepared formulations was examined by the MTT (3-(4,5-dimethylthiazolyl-2)-2,5-diphenyltetrazolium bromide) assay.[58] The cells were exposed to various concentrations of formulations for 48 h to determine the IC_{50} value (details in the ESI†).

2.6.3. Cellular uptake. Cellular uptake studies used coumarin-6 (CM6)-loaded formulations and free coumarin6 (CM6). 5×10^4 MDA-MB-231 cells were seeded in 12-well culture plates and incubated to adhere for 24 h. The cells were treated with CM6-loaded formulations equivalent to 2 μg ml^{-1} of CM6 and free CM6 dissolved in complete DMEM for six hours and incubated at 37 °C. To assess the role of EGFR in the endocytosis of nanoparticles, one of the wells received cetuximab pretreatment (30 min before the formulation treatment). Cells were washed with PBS and stained with Hoechst33342 (10 μg ml^{-1}) to incubate for 20 minutes for nuclear staining. Subsequently, the stained cells were washed with PBS, and images were captured using a green and blue channel EVOS FL Cell Imaging System. Further, a quantitative assessment of cellular uptake was performed using flow cytometry. Similar steps were performed up to the treatment stage. After the treatment with formulations, the cells were harvested in 1 mM EDTA and rinsed twice with PBS. The fluorescence intensity of CM6 was measured based on cell distribution using a CellQuest Calibur

flow cytometer (Becton Dickinson, USA).[59] The experiment was performed in triplicate.

2.6.4. Mitochondrial membrane potential and distribution pattern. Briefly, 5×10^4 viable MDA-MB-231 cells were seeded in 6-well cell culture plates and incubated for 24 h. Thereafter, the cells were treated with IC_{50} concentrations of formulations and incubated for 24 h. Further, the cells were stained with JC-1 dye at a 1 μM concentration in PBS and incubated for 30 minutes at 37 °C. Finally, the images were taken using a fluorescence microscope. The changes in mitochondrial membrane potential were validated quantitatively through flow cytometry. For quantitative detection, a similar experimental procedure was followed. The cells were harvested in 1 mM EDTA solution in PBS, stained with JC-1 dye, and analyzed using a flow cytometer.[60]

To evaluate the mitochondrial distribution pattern, a similar protocol was followed up to the treatment stage. Following treatment, the cells were stained with MitoTracker™ Red at a 1 μM concentration and the nuclei were counterstained using Hoechst33342 at a 10 μg ml^{-1} concentration for 30 minutes. After staining, the cells were again washed with PBS and the images were taken using a fluorescence microscope in phase contrast, blue and red channels.[61]

2.6.5. Apoptosis analysis using Hoechst33342/PI. Qualitative assessment of apoptosis was performed using Hoechst33342 and PI double staining. The MDA-MB-231 cells were plated on a 12-well cell culture plate for about 24 h. Thereafter, the cells were treated with IC_{50} concentrations of the formulations and incubated for 24 h. Further, PI (5 μl) and Hoechst33342 (10 μg ml^{-1}) were then added to the wells of the plate and then kept in the dark for about 30 minutes at 37 °C. The wells were washed with PBS and observed using a fluorescence microscope.[62]

For quantitative assessment of apoptosis, Alexa Fluor 488 Annexin V/PI double stained MDA-MB-231 cells were subjected to flow cytometry after being exposed to IC_{50} concentrations of the formulations. For this, 2×10^5 cells were seeded in 6-well cell culture plates and incubated for 24 h. Thereafter, the cells were treated with IC_{50} concentrations of the formulations. After 24 h, the cells were harvested in 1 mM EDTA in PBS (pH 7.4). Further, the treated and control cells were processed according to the manufacturer protocol for Alexa Fluor 488 Annexin V/PI staining (Thermo Fisher Scientific, Invitrogen Bioservices India Pvt. Ltd). After staining, the samples were analyzed by flow cytometry to evaluate apoptosis.[63]

2.7. *In vivo* studies

All *in vivo* experiments were carried out in accordance with the guidelines of CPCSEA (a Committee for the Purpose of Control and Supervision of Experiments on Animals, Regd. No. 2123/GO/Re/S/21/CPCSEA). The protocols for *in vivo* studies were approved by the Institutional Animal Ethics Committee (IAEC) (Approval number: IIT(BHU)/IAEC/2022/011) prior to the conduction of experiments. The animals were procured from the animal facility, Institute of Medical Sciences (BHU), Varanasi-221005 (542/GO/ReBi/S/02/CPCSEA).

2.7.1. Tumor induction in female SD rats. Female Sprague-Dawley rat pups of 5 weeks age (weight: 50–60 g) were used to develop a DMBA-induced mammary tumor model. After 1 week of conditioning under light and dark conditions for 12 h (age: 6 weeks), all the rats received 7,12-dimethylbenz(*a*)anthracene dissolved in corn oil (dose: 80 mg kg^{-1}) by subcutaneous injection into the mammary fat pad.[64,65] After 60 days, the tumors started to appear. The tumor volume was measured regularly. After 90–100 days of treatment with DMBA, the tumors exceeded a volume of 500 mm^3 and they are divided into various groups for studies mentioned below. The tumor volume was estimated using the formula:

$$V = \frac{4}{3}\pi(r^3)$$

where r indicates the average radius of the tumor tissue.

2.7.2. Pharmacokinetic studies. A pharmacokinetic study was performed on healthy female SD rats. The tumor-bearing rats were randomly distributed into 3 groups (n = 6). Groups 1 to 3 received micellar cabazitaxel (CBT), CSVE/HA/DTPA, and CSVE/HA/DTPA/Cmab, respectively, *via* intravenous injection into the tail vein at a dose equivalent to 10 mg kg^{-1} of cabazitaxel. The blood samples (200 μl) were collected under mild anesthetic conditions through *oculi choroideae* and centrifuged at 8000*g* for 5 min at −4 °C to separate the plasma. The liquid–liquid extraction method was used for plasma sample processing and analyzed by the developed analytical HPLC method. The plasma concentration–time profile was evaluated using the PK Solver add-in program to determine the pharmacokinetic parameters.

2.7.3. Biodistribution studies in tumor-bearing rats. To assess the drug distribution to majorly perfused organs, a biodistribution study was performed in tumor-bearing rats. The animals were divided into 3 groups (n = 12). Group 1 received cabazitaxel, group 2 received CSVE/HA/DTPA NP, and group 3 received CSVE/HA/DTPA/Cmab NP at a dose equivalent to 10 mg kg^{-1} of cabazitaxel *via* an intravenous route. After administration of the dose, the animals were euthanized at predetermined time intervals. Liver, lung, kidney, spleen, and tumor tissues were collected from the animals of each group after 2, 10, 24, and 48 hours of drug administration. 200 mg tissue sample was weighed and homogenized at −4 °C. The drug content from the homogenate was extracted using solvent extraction. A 1 : 1 (v/v) mixture of acetonitrile and methanol (200 μl) was added into the homogenate and mixed. The homogenate was separated by centrifugation and the supernatant was analyzed for drug concentration using the HPLC method.

2.7.4. Tumor regression analyses. The animals were divided into four groups (n = 5) and CSVE/HA/DTPA NP and CSVE/HA/DTPA/Cmab NP were administered through an intravenous route once every 3rd day at a dose equivalent to 10 mg kg^{-1} of CBT. The control and standard groups were treated with PBS and CBT, respectively. The tumor growth was measured every 7 days using a vernier caliper. The animal body weight was also measured throughout the study to check the

overall toxicity, and one group of healthy rats were used to estimate the weight change in normal rats.[66,67] Finally, the animals were killed after 28 days, and the tumor was collected for histological studies.

2.7.5. Survival analysis. For survival analysis, the tumor-bearing female SD rats were divided into four groups ($n = 5$) and healthy female SD rats in one group. The animals were treated with the same regimen mentioned in the tumor regression study. The survival study was carried out for up to 120 days. Finally, the dignified survival rate was evaluated using the Kaplan–Meier analysis.[68]

2.7.6. Assessment of acute toxicity by histological examination of the organs and tumor. After the tumor regression study, the rats were sacrificed. Major organs and tumors were collected. The collected samples were separately fixed in 10% paraformaldehyde (PBS buffer) for 12 h. The tissues were dehydrated, treated with xylene and embedded in paraffin blocks. The wax blocks were sectioned using a microtome (Leica) to obtain 5 μm thick sections. These sections were deparaffinized and then subsequently exposed to a hematoxylin and eosin staining protocol. The stained section was then dehydrated again and cleared with xylene, and mounted under a coverslip for visualization under a light microscope for histological changes.[69–71]

2.8. Statistical analysis

The results were reported as mean ± standard deviation (SD). The statistical significance of data was determined using the *t* test (non-parametric), one-way ANOVA and two-way ANOVA at *p* values of $*p < 0.05$, $**p < 0.01$, $***p < 0.001$, and $****p < 0.0001$. All statistical analyses were performed using GraphPad Prism 9.0.0 for Windows (GraphPad Software, San Diego, CA, USA).

3. Results and discussion

3.1. Formulation of CSVE-based nanoparticles

The prepared conjugate of CSO and VES (confirmed by NMR and FTIR; see details in the ESI,† Fig. S2 and S3) was used to prepare CSVE based nanoparticles. The presence of the same hydrophobic group (VES) and the net cationic and anionic charges of CSVE and TPGS-COOH, respectively, allows the formation of a stable micellar structure under aqueous conditions. The drug (CBT) was loaded in the stable hydrophobic core of the micellar structure which was further stabilized by ionic gelation through the addition of anionic hyaluronic acid. The stable hybrid nanoparticles formed were then crosslinked using DTPA to endow redox-responsive release behavior *via* carbodiimide chemistry. To impart cancer selective characteristics, the particles were surface-functionalized by conjugating Cmab to the carboxyl group of TPGS-COOH present on the surface of the nanoparticles.

The formulation composition and characterized parameters are given in Table 1. The hydrodynamic sizes determined by DLS of CSO/HA NP, CSVE/HA NP, CSVE/HA/DTPA NP, and CSVE/HA/DTPA/Cmab NP were 190 ± 23 nm, 179 ± 32 nm, 164 ± 29 nm, and 203 ± 43 nm, respectively. The amphiphilic nature of the CSVE conjugate combined with the identical hydrophobic segment (VES) of TPGS-COOH allows for the formation of a compactly packed micellar structure that leads to a lower size of CSVE/HA NP. The size of CSVE/HA/DTPA NP and CSVE/HA NP did not show major differences. However, the size of CSVE/HA/DTPA/Cmab NP exhibited a marked increase which may be attributed to the conjugation of Cmab on the surface of the nanoparticles.

However, the zeta potential (ζ) showed a different trend, with CSVE/HA/DTPA NP exhibiting the highest zeta potential, followed by CSVE/HA/DTPA/Cmab NP, CSO/HA NP, and the least in CSVE/HA NP (Table 1). This observation may be due to the higher amount of HA (an anionic polysaccharide) being used in CS/HA NP and CSVE/HA NP. The lower ζ in CSVE/HA NP than in CSO/HA NP may be due to the crosslinking *via* amide bond formation between chitosan and VES. Similar results have been previously reported where ζ has exhibited a reduction due to the conjugation of moieties with the amine groups of CSO.[27,72] The polydispersity index (PDI) of all formulations was less than 0.3, indicating monodisperse systems.

Additionally, TEM, SEM, and AFM images confirmed the formulation of well-structured spherical nanoparticles (Fig. 1). The particle sizes of CSO/HA NP, CSVE/HA NP, CSVE/HA/DTPA NP, and CSVE/HA/DTPA/Cmab NP observed by TEM were 170 ± 12 nm, 135 ± 19 nm, 126 ± 14 nm, and 175 ± 9 nm, respectively. The size observed in TEM was smaller than that observed in DLS which could be due to the difference in measurement conditions, as TEM analysis was employed for dried samples, while DLS was used to measure the hydrodynamic size of the particles and it takes into account the solvated water molecules on the surface.[73] The SAED pattern for all nanoparticles exhibited diffused rings, reflecting the

Table 1 Composition, particle size, polydispersity index (PDI), zeta potential and entrapment efficiency of various formulations

Formulation	Composition (mg)							Particle size (nm)	PDI	Zeta potential (ζ)	Entrapment efficiency (%)	Drug loading (%)
	CSO	CSVE	HA	TPGS-COOH	CBT	DTPA	Cmab					
CSO/HA NP	50	—	10	10	5	—	—	190 ± 23	0.265 ± 0.084	19.2 ± 2.35	53.24 ± 3.57	4.71 ± 0.19
CSVE/HA NP	—	50	10	10	5	—	—	179 ± 32	0.238 ± 0.071	16.4 ± 3.72	62.35 ± 2.91	5.06 ± 0.13
CSVE/HA/DTPA NP	—	50	5	10	5	12	—	164 ± 29	0.268 ± 0.045	12.1 ± 2.08	64.49 ± 3.53	4.98 ± 0.07
CSVE/HA/DTPA/Cmab NP	—	50	5	10	5	12	2.5	203 ± 43	0.167 ± 0.063	11.9 ± 2.57	63.77 ± 3.96	4.85 ± 0.14

*Results are shown as mean ± SD ($n = 6$).

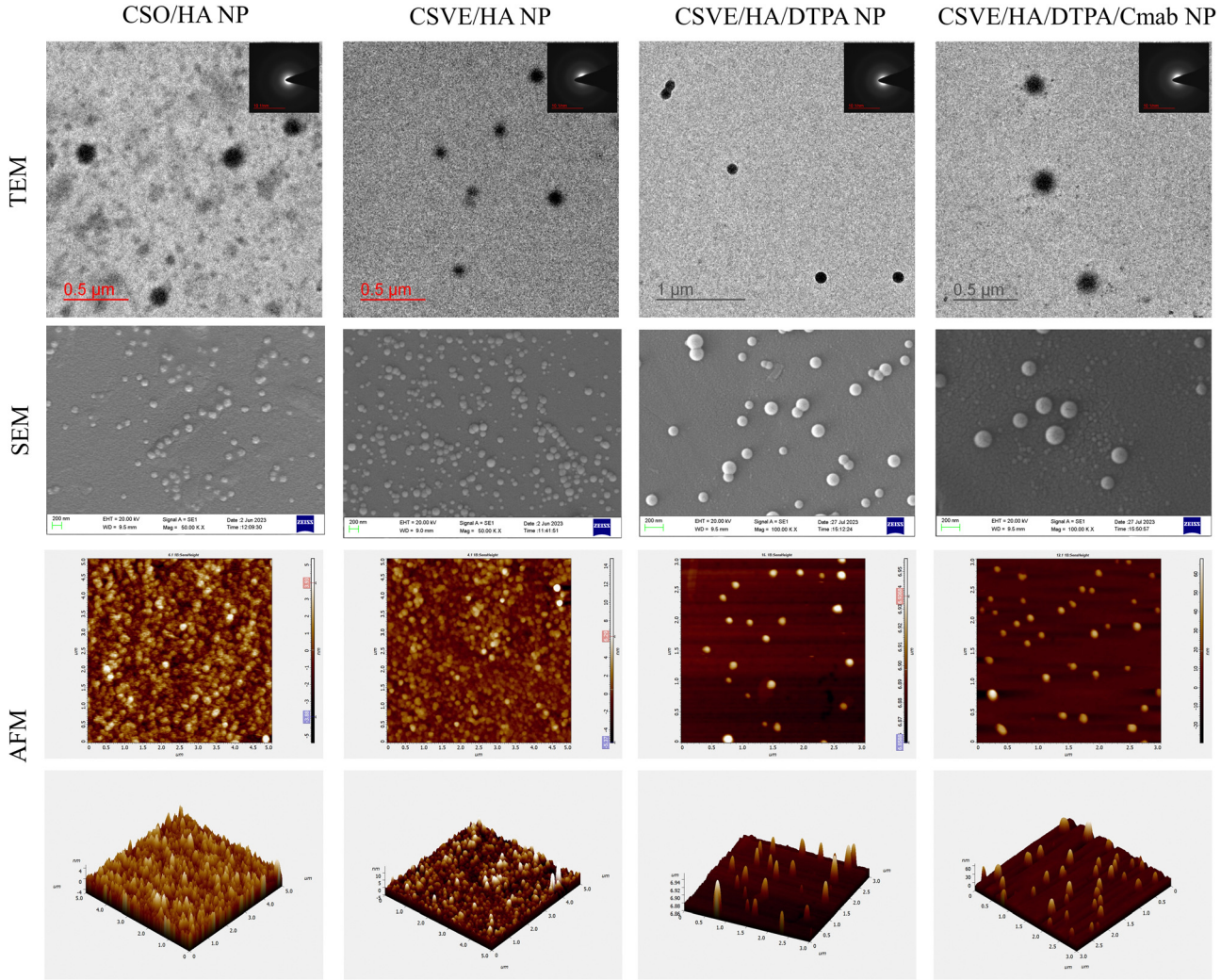

Fig. 1 Morphological assessment (TEM, SEM, and AFM) of CSO/HA NP, CSVE/HA NP, CSVE/HA/DTPA NP, and CSVE/HA/DTPA/Cmab NP.

amorphous state of nanoparticles. The particles of spherical anisotropy were confirmed by SEM (*i.e.*, CSO/HA NP: 145 ± 24, CSVE/HA NP: 136 ± 22 nm, CSVE/HA/DTPA NP: 117 ± 21 and CSVE/HA/DTPA/Cmab NP: 152 ± 29) and were of size similar to TEM results. TEM and SEM results followed the trend of DLS results, as desired. AFM images further confirmed the smooth surface spherical morphology of formulated nanoparticles. The results of SEM, TEM and AFM were in good correlation. The entrapment efficiency of formulated nanoparticles ranged between 53 and 65%. The nanoparticles formulated using the synthesized CSVE/HA had higher entrapment efficiency than CSO/HA nanoparticles. The higher entrapment efficiency of CSVE based formulations than that of CSO/HA NP may be attributed to the amphiphilic nature of the synthesized CSVE which may improve the drug loading capacity for hydrophobic drugs in the core of the micellar structure.[72] The degree of Cmab conjugation to the carboxyl group of TPGS-COOH was confirmed by the Bradford assay (details in the ESI†) which showed 71.635 ± 4.23% of added Cmab was conjugated onto the surface, indicating efficient surface functionalization.

3.2. Solid-state characterization (FTIR/XRD/DSC/XPS)

The FTIR spectra of CBT, CSVE, TPGS, HA, CSVE/HA NP, CSVE/HA/DTPA NP and CSVE/HA/DTPA/Cmab NP are shown in Fig. 2A (details in the ESI†). The characteristic peaks observed for CBT were similar to those previously reported for CBT.[74–76] The FTIR spectrum of CSVE/HA nanoparticles exhibited merged peaks of CSVE and HA and a similar trend was shown by CSVE/HA/DTPA NP and CSVE/HA/DTPA/Cmab NP. The characteristic peaks of crystalline CBT were masked by CSVE and HA, indicating complete encapsulation of the drug in the prepared nanoparticles.

The X-ray diffraction pattern (Fig. 2B) of CBT revealed its crystalline nature and its peaks were similar to previously reported peaks.[76] TPGS revealed two distinct peaks of a high intensity, while CSVE had an amorphous halo diffraction pattern with very small intensity peaks. CSVE/HA NP had peaks corresponding to TPGS and CSVE/HA/DTPA NP exhibited four peaks due to TPGS and the crosslinker. Meanwhile, the reduction in the intensity of these peaks in the case of CSVE/HA/DTPA/Cmab NP may be due to the surface

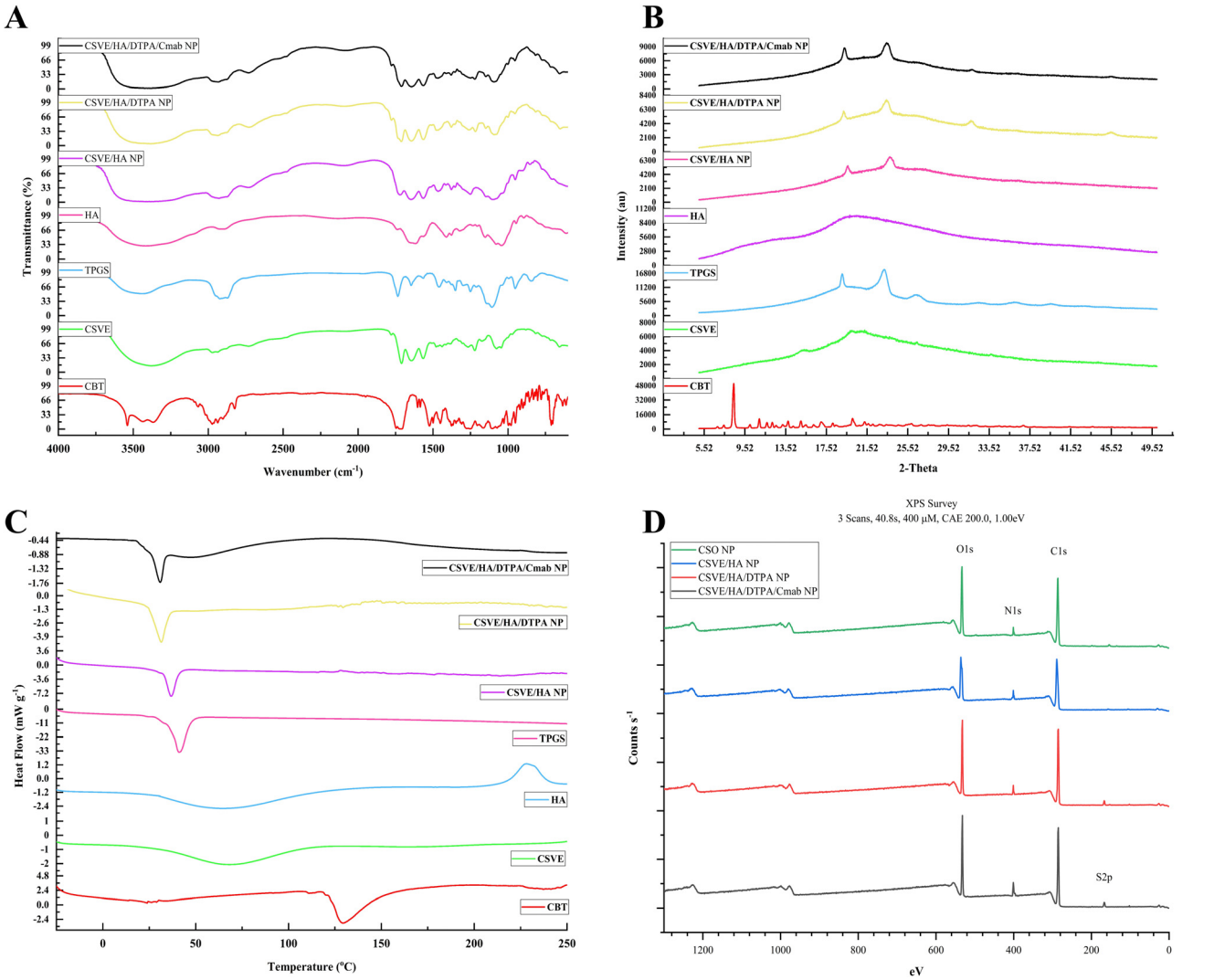

Fig. 2 Solid-state characterization; (A) FTIR, (B) XRD, and (C) DSC of cabazitaxel (CBT), CSVE, HA, TPGS, CSVE/HA NP, CSVE/HA/DTPA NP, and CSVE/HA/DTPA/Cmab NP. (D) XPS spectra of CSO NP, CSVE/HA NP, CSVE/HA/DTPA NP, and CSVE/HA/DTPA/Cmab NP.

conjugation of Cmab. The absence of CBT peaks in nanoparticles was due to the peak dominating effects of CSVE and HA (details in the ESI†).

The thermogram (Fig. 2C) of CBT showed a sharp endothermic peak which was absent in nanoparticles (details in the ESI†). The characteristic peak of TPGS however was present due to its presence on the nanoparticle surface with a minor shift attributed to nanosized particles.

The XPS spectra of CSO/HA NP and CSVE/HA NP showed signature C1s, N1s, and O1s peaks as shown in Fig. 2D. The presence of S2p and a marked increase in N1s signals indicate the successful DTPA mediated crosslinking and Cmab conjugation on the CSVE/HA/DTPA/Cmab NP surface (details in the ESI†).

3.3. Drug release study

The release study was conducted under conditions corresponding to the systemic circulation (pH 7.4), acidic tumor microenvironment (pH 5.5), and intracellular elevated ROS and reduced pH conditions (pH 5.5 + GSH). The redox responsive CSVE/HA/DTPA NP and CSVE/HA/DTPA/Cmab NP showed a marked increase in drug release in the presence of low pH and glutathione (GSH) (details in the ESI,† Fig. S5). Similar results were observed for a redox responsive nanoparticle prepared using DTPA due to cleavage by glutathione (GSH).[53] The release rate was highest in pH 5.5 + GSH (10 mM) followed by pH 5.5 and pH 7.4. Also, T_{50} values for CSVE/HA/DTPA/Cmab NP at pH 7.4, pH 5.5 and pH 5.5 + GSH were 15 h, 8.5 h, and 2.5 h, respectively, exhibiting a similar trend to CSVE/HA/DTPA NP (Fig. 3A). The pH-responsive trend in the release behavior of all the particles can be attributed to protonation of the amino groups on CS at lower pH values responsible for enhanced electrostatic repulsion and thus easy diffusion of the loaded drug from NPs.[72,77] However, the increased release of the drug in the media comprising low pH and GSH is due to the cleavage of the disulfide bonds of the crosslinker DTPA in response to GSH.[15,16,42] The GSH-responsive cleavage of the disulfide linkage was further confirmed using Ellman's reagent which

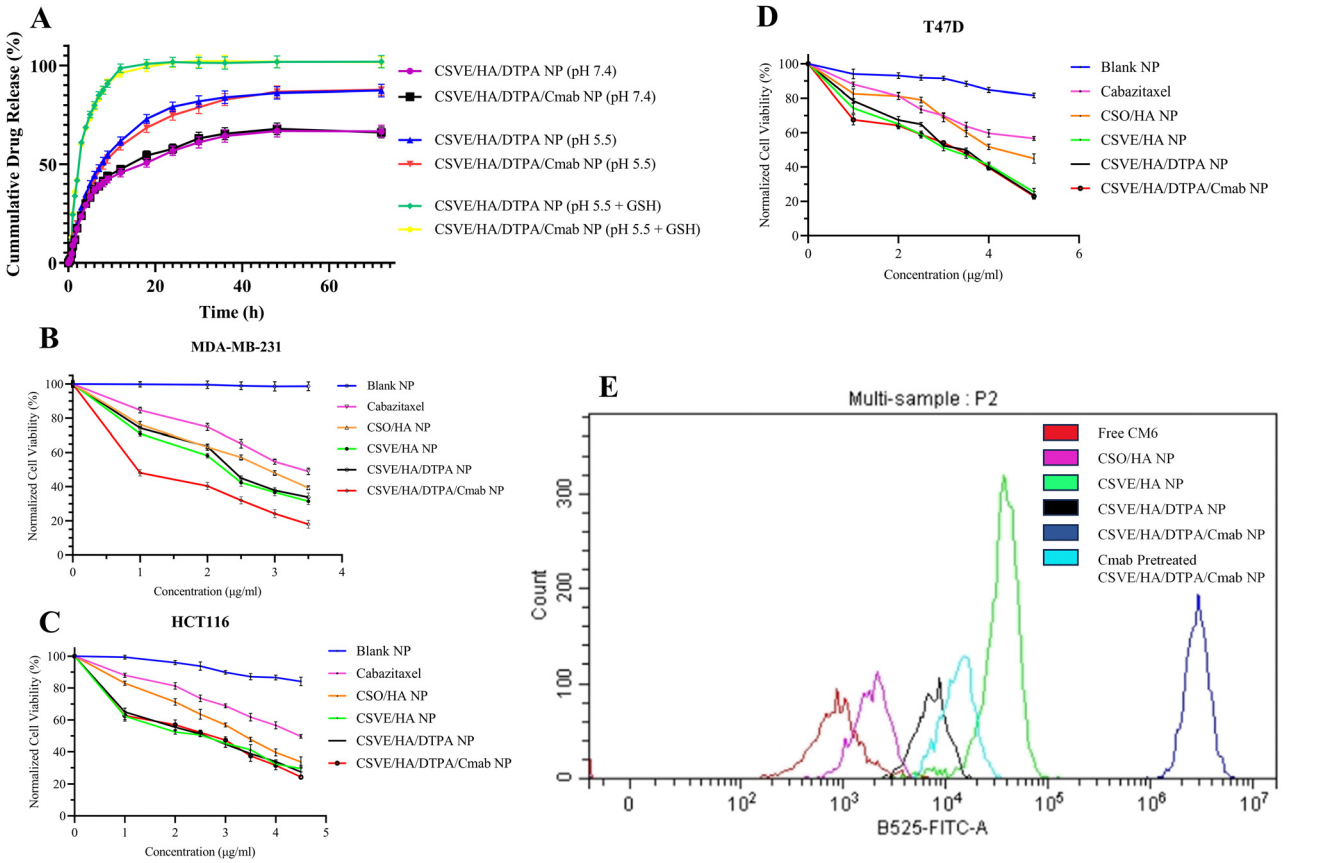

Fig. 3 (A) Drug release profiles of CSVE/HA/DTPA NP and CSVE/HA/DTPA/Cmab NP in pH 7.4 phosphate buffer saline, pH 5.5 acetate buffer, and pH 5.5 acetate buffer and glutathione (10 mM). (B) *In vitro* cell viability of MDA-MB-231 cells after treatment with cabazitaxel-loaded formulations for 24 h (n = 3). (C) *In vitro* cell viability of HCT116 cells after treatment with cabazitaxel-loaded formulations for 24 h (n = 3). (D) *In vitro* cell viability of T47D cells after treatment with cabazitaxel-loaded formulations for 24 h (n = 3). (E) Quantitative assessment of the intracellular uptake of green fluorescent CM6 in MDA-MB-231 cells treated with free CM6, CSO/HA NP, CSVE/HA NP, CSVE/HA/DTPA NP, CSVE/HA/DTPA/Cmab NP, and Cmab pre-treated CSVE/HA/DTPA/Cmab NP at a 0.2 μg ml^{-1} concentration of CM6 for 6 h using flow cytometry. The blue peak shows the highest cellular uptake of CM6 in CM6-loaded CSVE/HA/DTPA/Cmab NP treated cells compared to free CM6, CSO/HA NP, CSVE/HA NP, CSVE/HA/DTPA NP, and CSVE/HA/DTPA/Cmab NP treated cells.

showed a rapid release of the free thiol group in CSVE/HA/DTPA NP in the first 90 min when exposed to acetate buffer (pH 5.5) + GSH (details in the ESI,† Fig. S6). When the CSVE/HA/DTPA NP were exposed to acetate buffer (pH 5.5) + GSH, the disulfide linkage of DTPA cleaves to release the free thiol group, resulting in disassembly of the crosslinked polysaccharide nanoparticles consequently increasing the rate of cabazitaxel release.

The drug release kinetic modelling was also performed for CSVE/HA/DTPA/Cmab NP which followed Weibull/Gompertz at pH 7.4, logistic/probit at pH 5.5 and Weibull/logistic under pH 5.5 + GSH (details in the ESI,† Table S1). This suggested controlled drug release *via* a slow drug diffusion mechanism from spherical particles at pH 7.4.[78,79] At pH 5.5, an initial faster release followed by controlled drug release *via* a diffusion mechanism was observed.[80,81] This could be due to the pH responsiveness of the prepared nanoparticles that resulted in an initial faster release of the drug from the nanoparticle surface directly exposed to media followed by controlled release *via* drug diffusion from the core to the outer surface and then to the media. Meanwhile, in the case of pH 5.5 + GSH, the release was faster *via* an erosion and diffusion mechanism in response to GSH responsible for breakage of the linkage, loosening of the nanoparticle assembly and subsequent dissolution of the matrix and drug.[80,82]

The prepared nanoparticles were also investigated for storage stability (see details in the ESI,† Fig. S7). Slight changes in the particle size (hydrodynamic diameter), polydispersity index, zeta potential, and entrapment efficiency were observed. However, the differences were non-significant and thus the prepared nanoparticles were stable during their storage, suggesting their suitability for long-term use.

3.4. *In vitro* study

3.4.1. Cell viability assay. To investigate the cytotoxicity and antiproliferative activity of the formulations, MDA-MB-231 cells were exposed to various concentrations for 24 h and their IC_{50} values were determined (Fig. 3B–D). MTT data revealed that the formulations exhibit a substantial suppressive effect on the proliferation of the MDA-MB-231 cell line (details in the ESI†). CSVE/HA/DTPA/Cmab NP elicited the highest

inhibitory effect on MDA-MB-231 cells. The inhibitory effect of cabazitaxel showed a significant decline in T47D and HCT116 too, but the difference between CSVE/HA/DTPA NP and CSVE/HA/DTPA/Cmab NP was not significant. These results may be attributed to the increased internalization of CSVE/HA/DTPA/Cmab in MDA-MB-231 *via* EGFR mediated endocytosis. As HCT116 and T47D do not express EGFR up to the extent MDA-MB-231 does, the difference in the internalization of Cmab conjugated nanoparticles and nanoparticles without Cmab conjugation in these cells is not significant. To confirm this, a cellular uptake study was conducted in MDA-MB-231 cells.

3.4.2. Cellular uptake study. Fluorescence microscopy showed a higher cellular internalization potential of CSVE/HA NP compared to CSO/HA NP. This could be attributed to VES conjugation on the CSO backbone which renders amphiphilic character to the conjugate (CSVE) and thereby improves cellular localization *via* P-gp inhibition. Similar results were observed for DOX loaded chitosan-*g*-TPGS NP compared to only chitosan NPs.[72] Furthermore, CSVE/HA/DTPA NP obtained on crosslinking of CSVE/HA NP had slightly lower cellular uptake compared to CSVE/HA NP, but still higher compared to CSO/HA NP (Fig. 4). This could be due to the deformable structure of CSVE/HA NP which may have assisted in cellular internalization. In addition, CSVE/HA/DTPA/Cmab exhibited the highest cellular uptake in MDA-MB-231 cells, showing the maximum emission of green fluorescence in the cytoplasmic region than free CM6, CSO/HA NP, CSVE/HA NP, and CSVE/HA/DTPA NP. The higher cellular internalization was attributed to conjugated cetuximab directed uptake in MDA-MB-231 cells. The blocking study was further conducted to confirm the role of cetuximab in assisting targeted cellular internalization of nanoparticles. The study indicated diminished uptake upon pretreatment of cells with cetuximab leading to competitive binding of the antibody to EGFR causing hindrance in receptor-mediated endocytosis of CSVE/HA/DTPA/Cmab NP. Further, the quantitative analysis performed using flow cytometry yielded results that concurred with the above findings (Fig. 3E).

3.4.3. Mitochondrial membrane potential. Taxanes are reported to evoke a rapid decline in mitochondrial membrane potential. Microscopic evaluation for the detection of J-aggregates and J-monomers in MDA-MB-231 cells after treatment with the formulations indicated a significant effect on mitochondrial membrane potential. As shown in Fig. 5A, J-aggregates (distributed red fluorescence in the cytoplasmic region) were seen in control and blank formulation treated groups, indicating no alterations in mitochondrial membrane potential. The J-monomers (green fluorescent signals) were increasingly seen in the cabazitaxel and CSVE/HA/DTPA NP treated groups due to significant mitochondrial depolarization. However, the CSVE/HA/DTPA/Cmab NP treated group exhibited maximum J-monomer formation. Also, the blocking study showed a marked reduction in the J-monomer formation. The data conform with the cellular uptake studies, indicating that the receptor mediated endocytosis of CSVE/HA/DTPA/Cmab NP results in a superior anti-proliferative effect on the MDA-MB-231 cell line. Further, the mitochondrial membrane potential was also validated through flow cytometry, which also indicated a similar trend (Fig. 5B). In brief, 41.335% of the cell population showed decreased mitochondrial membrane potential in the CSVE/HA/DTPA/Cmab NP treated group, which was significantly higher (p value <0.001) than 33.665% in the CSVE/HA/DTPA NP group (Fig. 5C). In comparison, control cells showed 0.95% cell population with decreased mitochondrial membrane potential.

3.4.4. Study of mitochondrial distribution patterns. Mitochondria are the cell's powerhouse and produce ATP through oxidative phosphorylation which controls a variety of physiological activities in cells, and the pro-apoptotic signal of the cells can strongly correlate with mitochondrial dynamics and therefore impact its distribution pattern. According to several findings, cytotoxic materials that cause apoptosis can influence the mitochondrial distribution pattern. The distribution pattern of mitochondria in MDA-MB-231 cells stained with MitoTracker™ Red is shown in the microscopic image (Fig. 5D). Aggregation of mitochondria causes mitochondrial dysfunction, a positive regulator of apoptosis. The control treatment cells have consistent red fluorescence and a uniform distribution of mitochondria throughout the cytoplasm. MDA-MB-231 treated with 1 μg ml^{-1} concentrations of formulations induced aggregation of mitochondria towards perinuclear space and generated bright red fluorescence, indicating the involvement of an intrinsic mitochondrial pathway in apoptosis. The aggregation of mitochondria was significant in CSVE/HA/DTPA NP and CSVE/HA/DTPA/Cmab NP treated groups compared to control and CBT treated groups, with the CSVE/HA/DTPA/Cmab NP treated group exhibiting maximum aggregation. The Cmab pretreated group showed a reduction in mitochondrial aggregation indicating the role of EGFR in receptor mediated endocytosis of CSVE/HA/DTPA/Cmab NP.

3.4.5. Qualitative assessment of apoptosis. Hoechst33342 dye was used to observe the nuclear morphology of MDA-MB-231 cells treated with various formulations (Fig. 6A). After treatment with Hoechst33342 dye, the live cells usually emit blue fluorescence. Hoechst33342 mainly stains the chromatin present in cells. The apoptotic cells give a brighter blue fluorescence due to the condensed nature of chromatin compared to normal cells. On the other hand, PI is a DNA binding dye that is only permeant to dead cells and stain the cells only in the case of loss of plasma membrane integrity. In the case of control and blank formulations, only a low-bright blue fluorescence was observed denoting live cells with a highly integrated plasma membrane, while for CBT treatment groups, a brighter blue and red fluorescence was observed indicative of a highly condensed nucleus and the presence of apoptotic and necrosis cells. The brighter blue fluorescence of Hoechst33342 and red fluorescence of PI in CSVE/HA/DTPA NP and CSVE/HA/DTPA/Cmab NP treated groups revealed the presence of fragmented chromatin and loss of plasma membrane integrity, indicative of late apoptosis and cell death. The brighter fluorescence was representative of higher nuclear condensation and an increased number of apoptotic nuclei in nanoparticle treated groups.

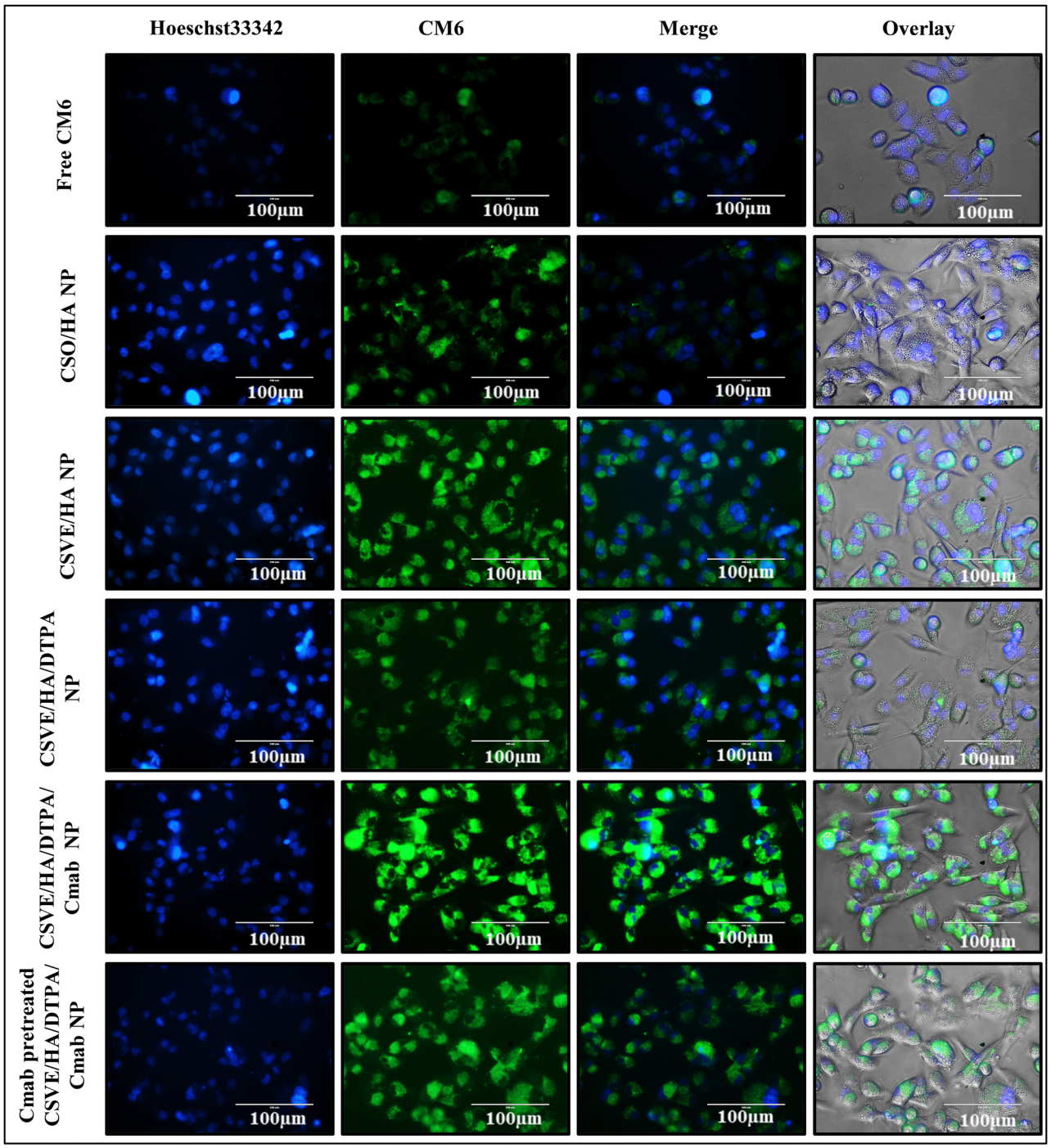

Fig. 4 Fluorescence microscopy images of MDA-MB-231 cells after 6 h incubation with the fluorescent CM6-loaded formulations. The blue fluorescence from DAPI channels shows Hoechst33342 stained nuclei, while the third column shows an overlay image of Hoechst and GFP. The fourth column represents an overlay image of phase contrast, GFP, and Hoechst33342. Each scale bar represents 100 µm. The GFP channel showed a higher level of green fluorescence in CM6 loaded CSVE/HA/DTPA/Cmab NP treated cells compared to free CM6 and CM6-loaded CSVE/HA/DTPA NP treated cells due to receptor-mediated cellular uptake of CM6 in the cytoplasm. The CM6-loaded CSVE/HA NP also exhibited superior intracellular localization of CM6 compared to CM6-loaded CSO/HA NP which may be attributed to the amphiphilic nature of the CSVE conjugate. The Cmab pretreated cells exhibited reduced uptake of CM6 which may be due to the competitive binding of Cmab to the EGFR.

3.4.6. Quantitative analysis of apoptosis. An initial event in apoptosis is detected by the disintegration of phospholipids and an undefined plasma layer. In the apoptotic cells, Annexin V binds to phosphatidylserine exposed on the extracellular layer of the plasma membrane which is otherwise located on the intracellular layer in normal cells. The necrotic and late apoptotic cells can also be stained with DNA-binding propidium iodide (PI) which does not penetrate across viable cells.

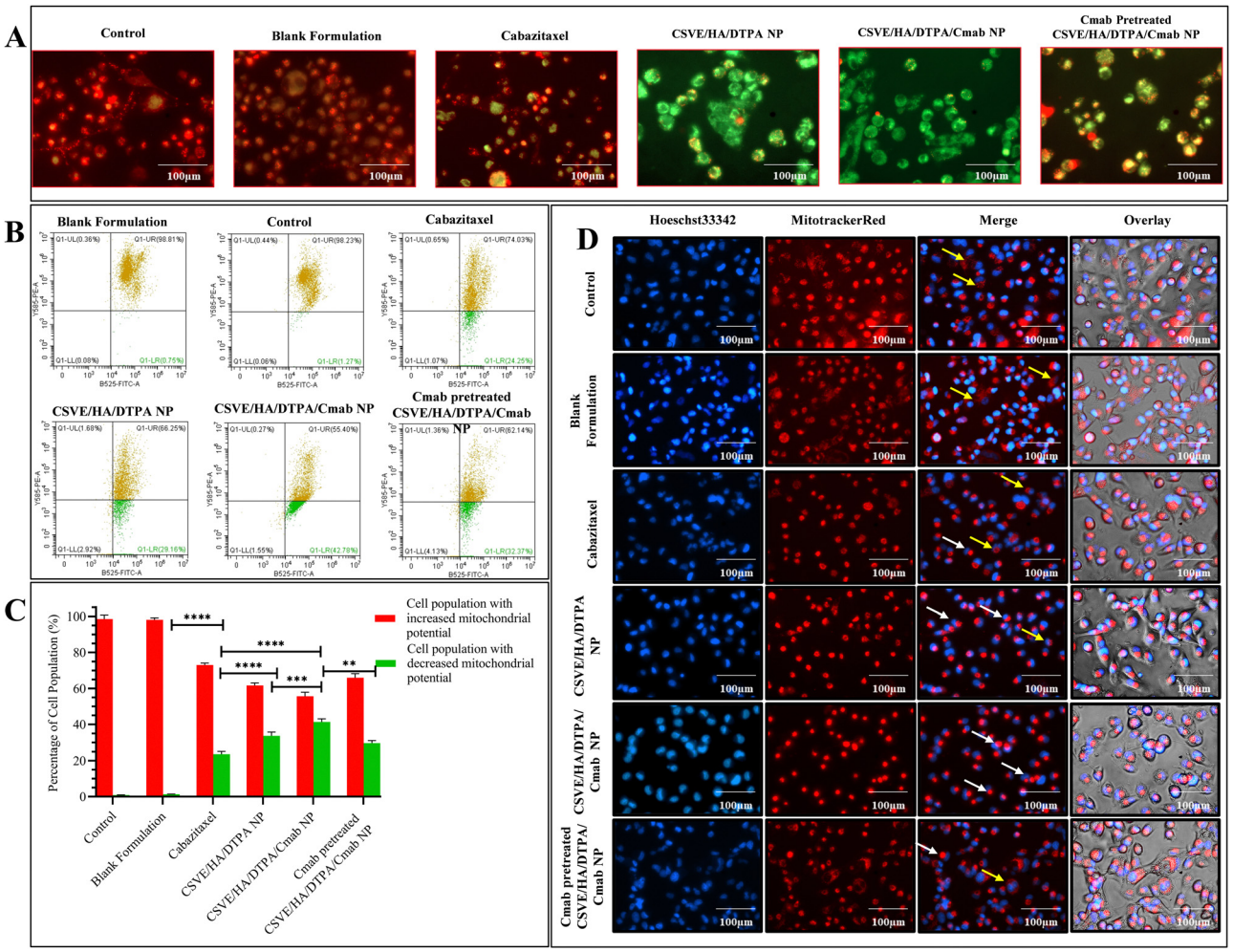

Fig. 5 (A) Assessment of mitochondrial membrane potential using JC-1 dye in control and treated MDA-MB-231 cells after treatment with cabazitaxel, CSVE/HA/DTPA NP, CSVE/HA/DTPA/Cmab NP, and Cmab pretreated CSVE/HA/DTPA/Cmab NP. The CSVE/HA/DTPA/Cmab NP treated group showed maximum depolarization (green fluorescence of JC-1 monomer) in cells. In contrast, the control group exhibited an accumulation of JC-1 monomers in negatively charged and energized normal mitochondria to spontaneously form J aggregates (red fluorescence). (B) and (C) Quantitative detection of mitochondrial membrane potential in MDA-MB-231 after treatment with the formulations through flow cytometry. The upper right and lower right quadrants represent cells with normal mitochondrial membrane potential and depolarized mitochondria, respectively. The CSVE/HA/DTPA/Cmab NP-treated cells showed maximum mitochondrial depolarization. (D) Pattern of mitochondrial distribution in MDA-MB-231 cells using MitoTracker™ Red after treatment with cabazitaxel, CSVE/HA/DTPA NP, CSVE/HA/DTPA/Cmab NP, and Cmab pretreated CSVE/HA/DTPA/Cmab NP. The uniform distribution of mitochondria was seen in control cells represented by the yellow arrow, while aggregated mitochondria were observed in the treatment group represented by the white arrows. The CSVE/HA/DTPA/Cmab treated cells showed the highest mitochondrial aggregation. Statistical analysis with significance: ****$p < 0.0001$, ***$p < 0.001$, and **$p < 0.01$.

Thus, the Annexin V–propidium iodide (PI) double labelling assay was used to demonstrate the induction of apoptosis in MDA-MB-231 cells after treatment with the formulations. As shown in the flow cytometry data analysis (Fig. 6B and C), the lower left quadrant represents the viable cells (Annexin V−/PI−cells) comprising 99.545% cell population in the control group which decreases to 30.09% in the CSVE/HA/DTPA/Cmab NP treated cells. The lower right quadrant represents early apoptotic cells (Annexin V+/PI−cells) which increased from 0.195% in the control cells to 38.65% in CSVE/HA/DTPA/Cmab NP treated cells. Also, the upper right (Annexin V+/PI+) and upper left quadrants (Annexin V−/PI+ cells) represent the late apoptotic cells and dead cells. The control group exhibits 0.17% and 0.09% cell populations in the upper right and left quadrants, respectively. The CSVE/HA/DTPA/Cmab NP-treated group showed 18.56% and 12.7% cell populations in the upper left and right quadrants, respectively. Although the dead cell population in the CSVE/HA/DTPA NP treated group was higher than that in the CSVE/HA/DTPA/Cmab NP treated group, the overall apoptotic and dead cell population was significantly (p value <0.001) higher in the latter.

3.5. *In vivo* study

3.5.1. Pharmacokinetics. The pharmacokinetic studies performed on SD female rats treated with CBT, CSVE/HA/DTPA NP, and CSVE/HA/DTPA/Cmab NP (Fig. 7). The nanoparticle dose

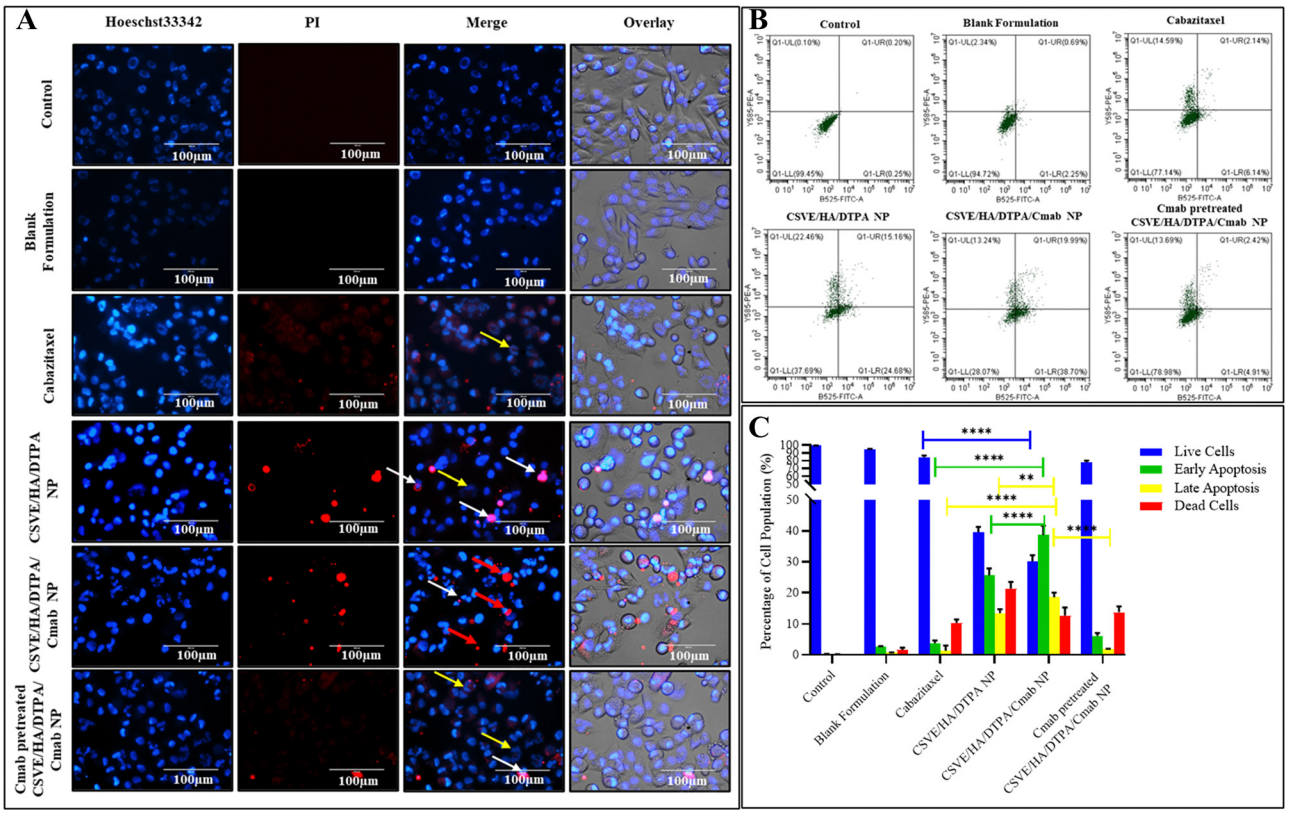

Fig. 6 (A) Combined images of Hoechst33342/PI-stained MDA-MB-231 cells after treatment with the formulations. The yellow, white, and red arrows represent early apoptotic, late apoptotic, and necrotic cells. Cells emitting blue fluorescence are Hoechst positive, while those with red fluorescence are PI positive. (B) and (C) Quantitative assessment of apoptosis by Annexin V/PI dual staining through flow cytometry in treated MDA-MB-231 cells. Annexin V/PI dual staining discriminates the percentage of live (lower left quadrant), early apoptotic (lower right quadrant), late apoptotic (upper right quadrant), and necrotic or dead (upper left quadrant) cells. Statistical analysis with significance: ****$p < 0.0001$ and **$p < 0.01$.

was equivalent to 10 mg kg^{-1} CBT administered *via* an intravenous route through the tail vein method. The pharmacokinetic parameters of the formulations generated from PKSolver add-in for Excel are presented in Table 2. A sustained-plasma concentration of CBT was observed in CSVE/HA/DTPA NP and CSVE/HA/DTPA/Cmab NP treated groups as compared to CBT. The C_{max} observed was highest with CBT (18 669 ng ml^{-1}) followed by CSVE/HA/DTPA/Cmab NP (18 369 ng ml^{-1}) and CSVE/HA/DTPA NP (18 119 ng ml^{-1}). However, the area under the curve for CSVE/HA/DTPA NP and CSVE/HA/DTPA/Cmab NP was three- to four-fold that of CBT. This could be due to the higher clearance of CBT from systemic circulation as compared to CSVE/HA/DTPA NP and CSVE/HA/DTPA/Cmab NP. A $t_{1/2}$ of only 11.34 h was observed for CBT, while $t_{1/2}$ values for CSVE/HA/DTPA NP and CSVE/HA/DTPA/Cmab NP were 30.74 h and 38.36 h, respectively. The mean retention time (MRT) of the drug was also shorter for CBT (13.56 h) than those for CSVE/HA/DTPA NP (40.40 h) and CSVE/HA/DTPA/Cmab NP (50.84 h). The results indicate that the prepared nanoparticles provided longer systemic circulation than CBT, allowing the sustained drug concentration to reach the target site and leverage its action, which could contribute to a better therapeutic response.

3.5.2. Biodistribution. The biodistribution study revealed a distinct pattern of higher drug concentration maintained in tumor tissues even after 48 hours of administration of dose (Fig. 7). The groups treated with CSVE/HA/DTPA/Cmab NP showed significantly (p value <0.001) higher drug permeation in tumor tissues after 2 h of dose administration. The drug concentration in tumor tissue further increased after 10 h and showed significantly higher levels even at 48 h. The CSVE/HA/DTPA NP also showed better tumor tissue permeation and retention than standard cabazitaxel. The concentration of cabazitaxel in the liver also showed a similar trend, indicating that the prepared nanoparticles were able to maintain the systemic concentration of cabazitaxel for a longer time. The distribution in the lungs however showed a similar concentration of cabazitaxel in all the groups at 2 h and 10 h, but higher concentrations in nanoparticle treated groups at 24 h and 48 h, indicating that sustained systemic levels of cabazitaxel loaded nanoparticles were achieved. The drug concentration in the kidneys was similar for all the treatment groups throughout the observation period with nanoparticles showing higher levels only at 48 h, probably due to the higher systemic levels of cabazitaxel maintained in these groups. The higher splenic concentration in the case of CSVE/HA/DTPA NP and CSVE/HA/DTPA/Cmab NP is due to their size. The nanocarriers are trapped in the spleen and result in a higher concentration of cabazitaxel in the tissue sample. The results indicate that the

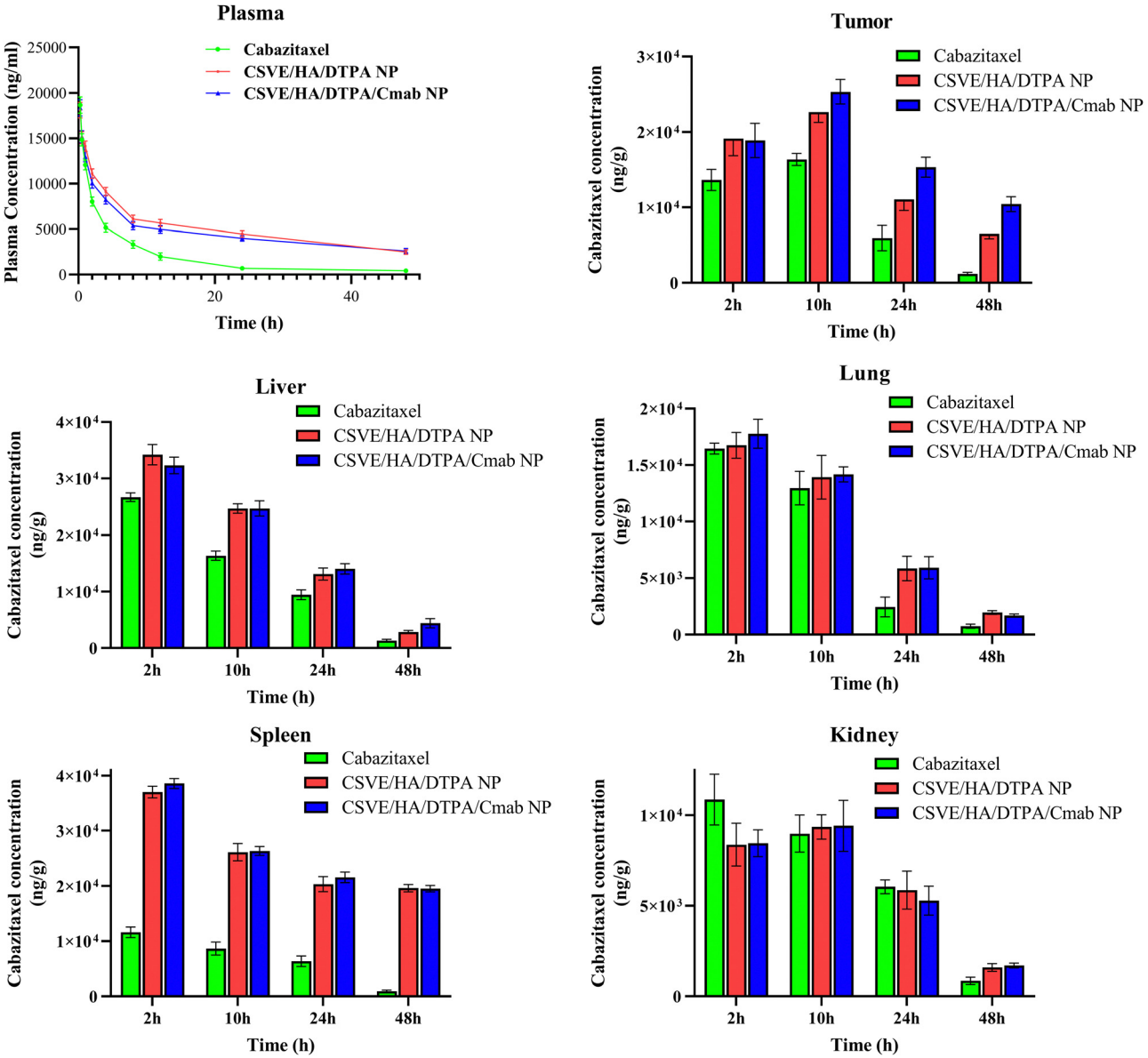

Fig. 7 Concentration of cabazitaxel in the plasma, tumor, liver, lungs, spleen and kidneys after intravenous administration of cabazitaxel, CSVE/HA/DTPA NP, and CSVE/HA/DTPA/Cmab NP.

Table 2 Pharmacokinetic parameters of various formulations determined from the plasma concentration *vs.* time plot

Parameters	Unit	Cabazitaxel	CSVE/HA/DTPA NP	CSVE/HA/DTPA/Cmab NP
$t_{1/2}$	h	11.3409	30.7382	38.3640
T_{max}	h	0.25	0.25	0.25
C_{max}	ng ml^{-1}	18 669.4540	18 119.0039	18 369.1091
C_0	ng ml^{-1}	23 473.1886	21 774.7884	22 217.6985
AUC 0-t	ng ml^{-1} h^{-1}	96 771.0839	247 526.4187	226 707.1421
AUC 0-inf_obs	ng ml^{-1} h^{-1}	103 915.5047	358 035.5039	369 966.0585
AUMC 0-inf_obs	ng ml^{-1} h^{-2}	1 408 825.881	14 463 854.26	18 809 769.52
MRT 0-inf_obs	H	13.5574	40.3978	50.8419
Cl_obs	(mg kg^{-1})/(ng ml^{-1}) h^{-1}	9.6232	2.7930	2.7029
F_{rel}		—	3.44	3.56

nanocarriers are able to maintain the drug concentration in systemic circulation for longer periods and selectively target the tumor tissues.

3.5.3. Tumor regression analyses. The body weights of all the animals were recorded after each treatment for the entire duration of tumor regression analysis (Fig. 8B). The normal SD

rats and control (untreated tumor bearing SD rats) group showed a gradual increase in body weight over the period of four weeks of treatment. The body weight of rats in the tumor bearing group treated with CBT reduced significantly ($p < 0.0001$) compared to normal and untreated tumor-bearing groups. The body weight of rats in the group treated with targeted nanoparticles was similar to normal and control groups (p = ns). However, the change in body weight was significant ($p < 0.0001$) in CBT treated groups compared to non-targeted and targeted groups. The non-significant change in the body weight of rats treated with targeted nanoparticles indicated a reduction in the toxicity of CBT due to selective accumulation in cancer cells, while the free CBT drug induced a significant reduction in body weight indicating systemic toxicity due to non-selective distribution (Fig. 8A). Tumors were collected after completion of treatment (Fig. 8D). The tumor volume significantly increased in untreated tumor-bearing rats, while groups treated with nanoparticles showed a marked reduction in tumor volume ($p < 0.0001$). The tumor volume reduction was highest in CSVE/HA/DTPA/Cmab NP followed by CSVE/HA/DTPA NP and CBT treated groups. The total tumor volume reduction of CSVE/HA/DTPA/Cmab NP was about 4.57-fold ($p = 0.0057$) and 15.23-fold ($p < 0.0001$) compared to CSVE/HA/DTPA NP and CBT treated groups.

3.5.4. Survival analysis. CSVE/HA/DTPA/Cmab NP showed a significant increase in the survival rate compared to the other groups (Fig. 8C). The median survival time of rats was 37, 56, 92 and >120 days in groups treated with control, CBT, CSVE/HA/DTPA NP, and CSVE/HA/DTPA/Cmab NP. The CBT treated group showed increased survival by 51% compared to the control group, while the CSVE/HA/DTPA NP and CSVE/HA/DTPA/Cmab NP treated groups showed higher survival by 148% and >230%, respectively. In comparison to CBT and non-targeted nanoparticle treated groups, the survival period for the targeted nanoparticle treated group was higher. This may be attributed to the higher efficiency of the prepared nanoparticles to selectively target cancer cells *via* receptor mediated endocytosis, thereby providing a better therapeutic effect.

3.5.5. Histopathology study. The H&E staining was used to determine the histological changes on tumor induction and their treatment with various formulations (Fig. 9A). Normal tissue exhibited normocellular structure, *i.e.* normal arrangement of fat tissue/adipocytes, lobules, and ducts with no signs of proliferated cancer cells.[71,83,84] Meanwhile, tumor bearing SD rats showed tissues rich in nuclear division showing invasive carcinoma (IC) with cells spread into surrounding stromal tissue (ST), disorganized and loosely connected. The immune cells may also have infiltrated into stromal tissue and several empty spaces formed in the stromal section.[70] The results revealed successful establishment of breast cancer (red arrows indicate the cancer cell area).[85] The carcinoma showed signs of increased proliferation and expansion of terminal lobular units (HLU), accompanied by expansion into surrounding fat tissue/adipocytes. The carcinoma showed dilated ducts with inspissated secretions (D), ductal carcinoma (DC), invasive cancer (IC), and mucin (yellow arrow).[84] The carcinoma also showed the presence of atrophy of glands with surrounding stromal fibrosis (fibroadenoma, F) and breast hyperplasia (H).[83] On treatment with CBT, although the breast hyperplasia area due to carcinoma decreased, there were still clear signs of cancer cells. Treatment with CSVE/HA/DTPA NP had effectively treated the breast cancer with only signs of remains of cancer cells. Although discontinuous membrane was still present in CSVE/HA/DTPA/Cmab NP treated groups, the

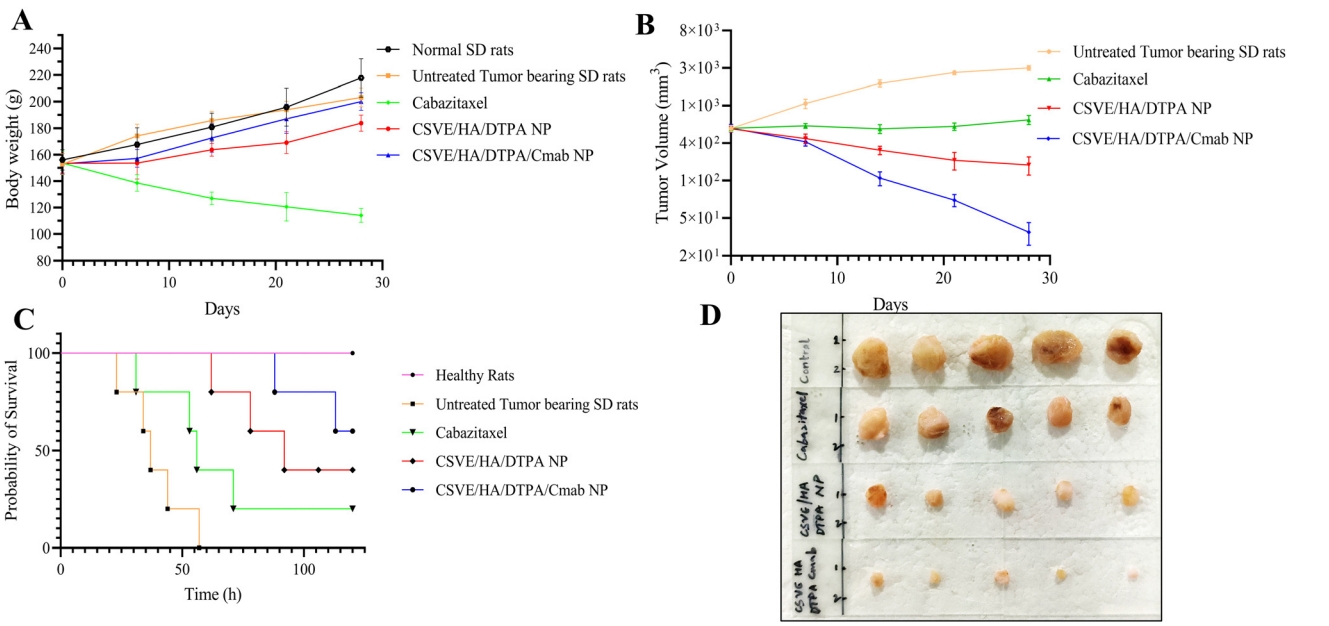

Fig. 8 (A) Body weight and (B) tumor volume of normal SD rats, tumor-bearing SD rats, and formulation treated tumor-bearing SD rats over the 28-day treatment period; (C) survival rates of tumor-bearing SD rats after treatment with formulations (day 0 represents the day of administration of the first dose after the tumor volume reached ~500 mm^3); (D) morphology of tumors harvested at the end of the study.

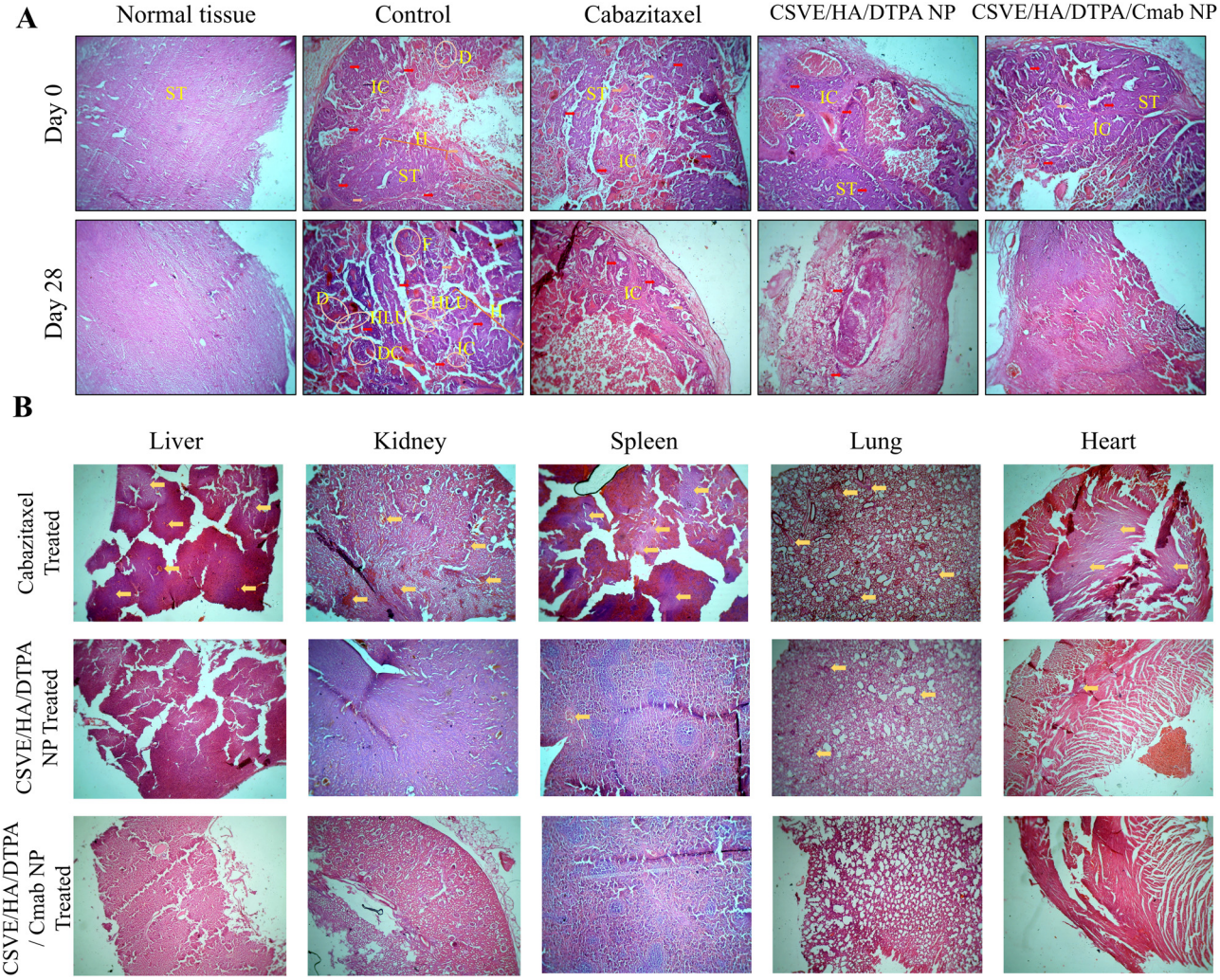

Fig. 9 (A) Histological assessment of tumors isolated from rats after the tumor regression study using H&E stain (magnification, 4×; scale bar, 100 μm). (B) Histological images of organ tissues after 28 days of treatment. Invasive carcinoma (IC), stromal tissue (ST), proliferated and expanded terminal lobular units (HLU), dilated ducts with inspissated secretions (D), ductal carcinoma (DC), mucin (yellow arrow), fibroadenoma (F) and breast hyperplasia (H).

carcinoma almost disappeared with complete disappearance of mucin and thick mass.[71]

The histological investigation of all major organs including the liver, kidneys, spleen, lungs and heart was also conducted to determine the safety of the prepared formulation as compared to free cabazitaxel. Free cabazitaxel showed major signs of toxicity (yellow arrow, Fig. 9B) in all major organs. In contrast, CSVE/HA/DTPA NP and CSVE/HA/DTPA/Cmab NP showed few or no signs of toxicity, suggesting the lower distribution of the free drug from nanoparticles to all major organs. Therefore, the prepared nanoformulations were safe and reduced the organ toxicity probably by minimizing the drug distribution to tissue and organs other than cancer.

4. Conclusion

Novel GSH-responsive cetuximab anchored chitosan/vitamin-E succinate conjugate-based hybrid nanoparticles were developed by an ionic gelation method. The particles exhibited spherical morphology with a sub-200 nm size, cationic surface charges, and redox responsive drug release. *In vitro* evaluations showed significantly superior cytotoxicity against MDA-MB-231 cells, enhanced cellular uptake, and reduced mitochondrial membrane potential in comparison to free CBT. The particles induced higher apoptosis than the free drug. The *in vivo* studies showed better performance of the nanoparticles than free CBT, with improved half-life, AUC, and MRT. Tumor regression analysis, survival and histological analysis indicated that CSVE/HA/DTPA/Cmab NP treated groups elicited better treatment response and lesser signs of toxicity in tissues than the free drug. Overall, the prepared hybrid receptor-targeted nanoparticles responsive to intracellular ROS species like GSH have immense potential as a targeted anticancer drug delivery platform. However, these preliminary findings should be extrapolated to extensive and advanced investigation to determine the clinical viability of CSVE/HA/DTPA/Cmab NP as an effective treatment modality for breast cancer. The major hurdle towards

the translational potential of the tumor microenvironment responsive system is the variable response of the system over the wide range of stimuli from various microenvironments seen in different cancers. The ability of the nanocarrier to release therapeutics in response to a broader range of redox stimuli in *in vitro* and *in vivo* settings may be studied in the future.

Data availability

All data are included in the manuscript.

Conflicts of interest

There are no conflicts to declare.

Acknowledgements

The authors gratefully acknowledge the Ministry of Education, Govt. of India and IIT (BHU), Varanasi, India for providing teaching assistantship. The authors are thankful to the Central Instrumentation Facility (CIF), IIT (BHU), Varanasi and SATHI-BHU, Varanasi for providing the instrumental support for the characterization of the formulations. The author BK acknowledges Banaras Hindu University for providing funding under the IoE scheme (File No. R/Dev/D/IoE/Incentive/2021-22/32449). The graphical abstract was made using elements from Servier Medical Art by Servier licensed under a Creative Commons Attribution 3.0 Unported License (**https://smart.servier.com**).

References

1 H. Sung, J. Ferlay, R. L. Siegel, M. Laversanne, I. Soerjomataram, A. Jemal and F. Bray, Global Cancer Statistics 2020: GLOBOCAN Estimates of Incidence and Mortality Worldwide for 36 Cancers in 185 Countries, *CA-Cancer J. Clin.*, 2021, **71**, 209–249, DOI: **10.3322/caac.21660**.

2 M. T. Manzari, Y. Shamay, H. Kiguchi, N. Rosen, M. Scaltriti and D. A. Heller, Targeted drug delivery strategies for precision medicines, *Nat. Rev. Mater.*, 2021, **6**, 351–370, DOI: **10.1038/s41578-020-00269-6**.

3 M. J. Mitchell, M. M. Billingsley, R. M. Haley, M. E. Wechsler, N. A. Peppas and R. Langer, Engineering precision nanoparticles for drug delivery, *Nat. Rev. Drug Discovery*, 2021, **20**, 101–124, DOI: **10.1038/s41573-020-0090-8**.

4 D. Fan, Y. Cao, M. Cao, Y. Wang, Y. Cao and T. Gong, Nanomedicine in cancer therapy, *Signal Transduction Targeted Ther.*, 2023, **8**, 1–34, DOI: **10.1038/s41392-023-01536-y**.

5 P. Foroozandeh and A. A. Aziz, Insight into Cellular Uptake and Intracellular Trafficking of Nanoparticles, *Nanoscale Res. Lett.*, 2018, **13**, 339, DOI: **10.1186/s11671-018-2728-6**.

6 M. E. Davis, Z. (Georgia) Chen and D. M. Shin, Nanoparticle therapeutics: an emerging treatment modality for cancer, *Nat. Rev. Drug Discovery*, 2008, **7**, 771–782, DOI: **10.1038/nrd2614**.

7 D. A. Richards, A. Maruani and V. Chudasama, Antibody fragments as nanoparticle targeting ligands: a step in the right direction, *Chem. Sci.*, 2016, **8**, 63–77, DOI: **10.1039/C6SC02403C**.

8 E. da S. Santos, K. A. B. Nogueira, L. C. C. Fernandes, J. R. P. Martins, A. V. F. Reis, J. de, B. V. Neto, I. J. da, S. Júnior, C. Pessoa, R. Petrilli and J. O. Eloy, EGFR targeting for cancer therapy: Pharmacology and immunoconjugates with drugs and nanoparticles, *Int. J. Pharm.*, 2021, **592**, 120082, DOI: **10.1016/j.ijpharm.2020.120082**.

9 D. Geethakumari, A. Bhaskaran Sathyabhama, K. Raji Sathyan, D. Mohandas, J. V. Somasekharan and S. T. Puthiyedathu, Folate functionalized chitosan nanoparticles as targeted delivery systems for improved anticancer efficiency of cytarabine in MCF-7 human breast cancer cell lines, *Int. J. Biol. Macromol.*, 2022, **199**, 150–161, DOI: **10.1016/j.ijbiomac.2021.12.070**.

10 S. Idoudi, Y. Hijji, T. Bedhiafi, H. M. Korashy, S. Uddin, M. Merhi, S. Dermime and N. Billa, A novel approach of encapsulating curcumin and succinylated derivative in mannosylated-chitosan nanoparticles, *Carbohydr. Polym.*, 2022, **297**, 120034, DOI: **10.1016/j.carbpol.2022.120034**.

11 S. Chen, X. Ji, M. Zhao, J. Jin, H. Zhang and L. Zhao, Construction of chitooligosaccharide-based nanoparticles of pH/redox cascade responsive for co-loading cyclosporin A and AZD9291, *Carbohydr. Polym.*, 2022, **291**, 119619, DOI: **10.1016/j.carbpol.2022.119619**.

12 L. Jia, Z. Li, D. Zheng, Z. Li and Z. Zhao, A targeted and redox/pH-responsive chitosan oligosaccharide derivatives based nanohybrids for overcoming multidrug resistance of breast cancer cells, *Carbohydr. Polym.*, 2021, **251**, 117008, DOI: **10.1016/j.carbpol.2020.117008**.

13 P. Song, Z. Lu, T. Jiang, W. Han, X. Chen and X. Zhao, Chitosan coated pH/redox-responsive hyaluronic acid micelles for enhanced tumor targeted co-delivery of doxorubicin and siPD-L1, *Int. J. Biol. Macromol.*, 2022, **222**, 1078–1091, DOI: **10.1016/j.ijbiomac.2022.09.245**.

14 M. Zhao, P. Li, H. Zhou, L. Hao, H. Chen and X. Zhou, pH/redox dual responsive from natural polymer-based nanoparticles for on-demand delivery of pesticides, *Chem. Eng. J.*, 2022, **435**, 134861, DOI: **10.1016/j.cej.2022.134861**.

15 A. Sood, A. Gupta, R. Bharadwaj, P. Ranganath, N. Silverman and G. Agrawal, Biodegradable disulfide crosslinked chitosan/stearic acid nanoparticles for dual drug delivery for colorectal cancer, *Carbohydr. Polym.*, 2022, **294**, 119833, DOI: **10.1016/j.carbpol.2022.119833**.

16 F. Wang, J. Li, C. Chen, H. Qi, K. Huang and S. Hu, Preparation and synergistic chemo-photothermal therapy of redox-responsive carboxymethyl cellulose/chitosan complex nanoparticles, *Carbohydr. Polym.*, 2022, **275**, 118714, DOI: **10.1016/j.carbpol.2021.118714**.

17 Q. Li, X. Liu, C. Yan, B. Zhao, Y. Zhao, L. Yang, M. Shi, H. Yu, X. Li and K. Luo, Polysaccharide-Based Stimulus-Responsive Nanomedicines for Combination Cancer Immunotherapy, *Small*, 2023, **19**, 2206211, DOI: **10.1002/smll.202206211**.

18 M. Li, Y. Zhao, W. Zhang, S. Zhang and S. Zhang, Multiple-therapy strategies via polysaccharides-based nano-systems

in fighting cancer, *Carbohydr. Polym.*, 2021, **269**, 118323, DOI: 10.1016/j.carbpol.2021.118323.

19 S. Mizrahy and D. Peer, Polysaccharides as building blocks for nanotherapeutics, *Chem. Soc. Rev.*, 2012, **41**, 2623–2640, DOI: 10.1039/C1CS15239D.

20 F. A. Taher, S. A. Ibrahim, A. A. El-Aziz, M. F. Abou El-Nour, M. A. El-Sheikh, N. El-Husseiny and M. M. Mohamed, Anti-proliferative effect of chitosan nanoparticles (extracted from crayfish Procambarus clarkii, Crustacea: Cambaridae) against MDA-MB-231 and SK-BR-3 human breast cancer cell lines, *Int. J. Biol. Macromol.*, 2019, **126**, 478–487, DOI: 10.1016/j.ijbiomac.2018.12.151.

21 H. Amin, M. A. Amin, S. K. Osman, A. M. Mohammed and G. Zayed, Chitosan nanoparticles as a smart nanocarrier for gefitinib for tackling lung cancer: Design of experiment and *in vitro* cytotoxicity study, *Int. J. Biol. Macromol.*, 2023, **246**, 125638, DOI: 10.1016/j.ijbiomac.2023.125638.

22 F. V. Ataabadi, F. Oveissi, M. Etebari and A. Taheri, Preparation of chitosan nanoparticles for simultaneous drug delivery of dacarbazine and enoxaparin in melanoma, *Carbohydr. Polym.*, 2023, **316**, 121041, DOI: 10.1016/j.carbpol.2023.121041.

23 P. Manivasagan, S. Bharathiraja, N. Q. Bui, I. G. Lim and J. Oh, Paclitaxel-loaded chitosan oligosaccharide-stabilized gold nanoparticles as novel agents for drug delivery and photoacoustic imaging of cancer cells, *Int. J. Pharm.*, 2016, **511**, 367–379, DOI: 10.1016/j.ijpharm.2016.07.025.

24 F.-Q. Hu, X. Wu, Y.-Z. Du, J. You and H. Yuan, Cellular uptake and cytotoxicity of shell crosslinked stearic acid-grafted chitosan oligosaccharide micelles encapsulating doxorubicin, *Eur. J. Pharm. Biopharm.*, 2008, **69**, 117–125, DOI: 10.1016/j.ejpb.2007.09.018.

25 Y.-Z. Du, L. Wang, H. Yuan and F.-Q. Hu, Linoleic acid-grafted chitosan oligosaccharide micelles for intracellular drug delivery and reverse drug resistance of tumor cells, *Int. J. Biol. Macromol.*, 2011, **48**, 215–222, DOI: 10.1016/j.ijbiomac.2010.11.005.

26 J. Dou, H. Zhang, X. Liu, M. Zhang and G. Zhai, Preparation and evaluation *in vitro* and *in vivo* of docetaxel loaded mixed micelles for oral administration, *Colloids Surf., B*, 2014, **114**, 20–27, DOI: 10.1016/j.colsurfb.2013.09.010.

27 Y. Chen, S. Feng, W. Liu, Z. Yuan, P. Yin and F. Gao, Vitamin E Succinate-Grafted-Chitosan Oligosaccharide/RGD-Conjugated TPGS Mixed Micelles Loaded with Paclitaxel for U87MG Tumor Therapy, *Mol. Pharmaceutics*, 2017, **14**, 1190–1203, DOI: 10.1021/acs.molpharmaceut.6b01068.

28 A. M. Itoo, M. Paul, B. Ghosh and S. Biswas, Oxaliplatin delivery via chitosan/vitamin E conjugate micelles for improved efficacy and MDR-reversal in breast cancer, *Carbohydr. Polym.*, 2022, **282**, 119108, DOI: 10.1016/j.carbpol.2022.119108.

29 Y. Yu, L. Hou, H. Song, P. Xu, Y. Sun and K. Wu, Akt/AMPK/mTOR pathway was involved in the autophagy induced by vitamin E succinate in human gastric cancer SGC-7901 cells, *Mol. Cell. Biochem.*, 2017, **424**, 173–183, DOI: 10.1007/s11010-016-2853-4.

30 L. Liang and L. Qiu, Vitamin E succinate with multiple functions: A versatile agent in nanomedicine-based cancer therapy and its delivery strategies, *Int. J. Pharm.*, 2021, **600**, 120457, DOI: 10.1016/j.ijpharm.2021.120457.

31 T. Weber, H. Dalen, L. Andera, A. Nègre-Salvayre, N. Augé, M. Sticha, A. Lloret, A. Terman, P. K. Witting, M. Higuchi, M. Plasilova, J. Zivny, N. Gellert, C. Weber and J. Neuzil, Mitochondria Play a Central Role in Apoptosis Induced by α-Tocopheryl Succinate, an Agent with Antineoplastic Activity: Comparison with Receptor-Mediated Pro-Apoptotic Signaling, *Biochemistry*, 2003, **42**, 4277–4291, DOI: 10.1021/bi020527j.

32 R. G. Tuguntaev, S. Chen, A. S. Eltahan, A. Mozhi, S. Jin, J. Zhang, C. Li and X.-J. Liang, P-gp Inhibition and Mitochondrial Impairment by Dual-Functional Nanostructure Based on Vitamin E Derivatives To Overcome Multidrug Resistance, *ACS Appl. Mater. Interfaces*, 2017, **9**, 16900–16912, DOI: 10.1021/acsami.7b03877.

33 F. A. Boratto, M. S. Franco, A. L. B. Barros, G. D. Cassali, A. Malachias, L. A. M. Ferreira and E. A. Leite, Alpha-tocopheryl succinate improves encapsulation, pH-sensitivity, antitumor activity and reduces toxicity of doxorubicin-loaded liposomes, *Eur. J. Pharm. Sci.*, 2020, **144**, 105205, DOI: 10.1016/j.ejps.2019.105205.

34 W. Jiang, Q. Fan, J. Wang, B. Zhang, T. Hao, Q. Chen, L. Li, L. Chen, H. Cui and Z. Li, PEGylated phospholipid micelles containing D-α-tocopheryl succinate as multifunctional nanocarriers for enhancing the antitumor efficacy of doxorubicin, *Int. J. Pharm.*, 2021, **607**, 120979, DOI: 10.1016/j.ijpharm.2021.120979.

35 L. Manthalkar, S. Bhattacharya, K. Hatware, P. Sreelaya, D. Shah, A. Jain and N. Phatak, Fabrication of D-α-tocopheryl polyethylene glycol 1000 succinates and human serum albumin conjugated chitosan nanoparticles of bosutinib for colon targeting application; *in vitro–in vivo* investigation, *Int. J. Biol. Macromol.*, 2023, **253**, 127531, DOI: 10.1016/j.ijbiomac.2023.127531.

36 S. Behzadi, V. Serpooshan, W. Tao, M. A. Hamaly, M. Y. Alkawareek, E. C. Dreaden, D. Brown, A. M. Alkilany, O. C. Farokhzad and M. Mahmoudi, Cellular uptake of nanoparticles: journey inside the cell, *Chem. Soc. Rev.*, 2017, **46**, 4218–4244 https://pubs.rsc.org/en/content/articlehtml/2017/cs/c6cs00636a (accessed November 27, 2023).

37 M. A. Anbardan, S. Alipour, G. R. Mahdavinia and P. F. Rezaei, Synthesis of magnetic chitosan/hyaluronic acid/κ-carrageenan nanocarriers for drug delivery, *Int. J. Biol. Macromol.*, 2023, **253**, 126805, DOI: 10.1016/j.ijbiomac.2023.126805.

38 Z. Lu, L. Ma, L. Mei, K. Ren, M. Li, L. Zhang, X. Liu and Q. He, Micellar nanoparticles inhibit the postoperative inflammation, recurrence and pulmonary metastasis of 4T1 breast cancer by blocking NF-κB pathway and promoting MDSCs depletion, *Int. J. Pharm.*, 2022, **628**, 122303, DOI: 10.1016/j.ijpharm.2022.122303.

39 H. Wang, P. Agarwal, S. Zhao, R. X. Xu, J. Yu, X. Lu and X. He, Hyaluronic acid-decorated dual responsive nanoparticles of Pluronic F127, PLGA, and chitosan for targeted co-delivery of doxorubicin and irinotecan to eliminate cancer stem-like cells, *Biomaterials*, 2015, **72**, 74–89, DOI: 10.1016/j.biomaterials.2015.08.048.

40 T. Nalini, S. K. Basha, A. M. Sadiq and V. S. Kumari, *In vitro* cytocompatibility assessment and antibacterial effects of quercetin encapsulated alginate/chitosan nanoparticle, *Int. J. Biol. Macromol.*, 2022, **219**, 304–311, DOI: **10.1016/j.ijbiomac.2022.08.007**.

41 Y. Zhang, R. Ma, C. You, X. Leng, D. Wang, S. Deng, B. He, Z. Guo, Z. Guan, H. Lei, J. Yu, Q. Zhou, J. Xing and Y. Dong, Hyaluronic acid modified oral drug delivery system with mucoadhesiveness and macrophage-targeting for colitis treatment, *Carbohydr. Polym.*, 2023, **313**, 120884, DOI: **10.1016/j.carbpol.2023.120884**.

42 H. Vakilzadeh, J. Varshosaz, M. Dinari, M. Mirian, V. Hajhashemi, N. Shamaeizadeh and H. M. Sadeghi, Smart redox-sensitive micelles based on chitosan for dasatinib delivery in suppressing inflammatory diseases, *Int. J. Biol. Macromol.*, 2023, **229**, 696–712, DOI: **10.1016/j.ijbiomac.2022.12.111**.

43 J. Wang, J. Liu, D.-Q. Lu, L. Chen, R. Yang, D. Liu and B. Zhang, Diselenide-crosslinked carboxymethyl chitosan nanoparticles for doxorubicin delivery: Preparation and *in vivo* evaluation, *Carbohydr. Polym.*, 2022, **292**, 119699, DOI: **10.1016/j.carbpol.2022.119699**.

44 A. K. Pandey, N. Piplani, T. Mondal, A. Katranidis and J. Bhattacharya, Efficient delivery of hydrophobic drug, Cabazitaxel, using Nanodisc: A nano sized free standing planar lipid bilayer, *J. Mol. Liq.*, 2021, **339**, 116690, DOI: **10.1016/j.molliq.2021.116690**.

45 C. Villanueva, F. Bazan, S. Kim, M. Demarchi, L. Chaigneau, A. Thiery-Vuillemin, T. Nguyen, L. Cals, E. Dobi and X. Pivot, Cabazitaxel: a novel microtubule inhibitor, *Drugs*, 2011, **71**, 1251–1258, DOI: **10.2165/11591390-000000000-00000**.

46 C. J. Paller and E. S. Antonarakis, Cabazitaxel: a novel second-line treatment for metastatic castration-resistant prostate cancer, *DDDT*, 2011, **5**, 117–124, DOI: **10.2147/DDDT.S13029**.

47 G. Nightingale and J. Ryu, Cabazitaxel (jevtana): a novel agent for metastatic castration-resistant prostate cancer, *P T*, 2012, **37**, 440–448.

48 A. Koutras, F. Zagouri, G.-A. Koliou, E. Psoma, I. Chryssogonidis, G. Lazaridis, D. Tryfonopoulos, A. Kotsakis, N. K. Kentepozidis and E. Razis, Phase 2 study of Cabazitaxel as second-line treatment in patients with HER2-negative metastatic breast cancer previously treated with taxanes—a Hellenic Cooperative Oncology Group (HeCOG) Trial, *Br. J. Cancer*, 2020, **123**, 355–361 **https://www.nature.com/articles/s41416-020-0909-4** (accessed November 27, 2023).

49 N. Kommineni, S. Mahira, A. J. Domb and W. Khan, Cabazitaxel-loaded nanocarriers for cancer therapy with reduced side effects, *Pharmaceutics*, 2019, **11**, 141 **https://www.mdpi.com/1999-4923/11/3/141** (accessed August 19, 2024.

50 Y. Sun, R. J. Lee, F. Meng, G. Wang, X. Zheng, S. Dong and L. Teng, Microfluidic self-assembly of high cabazitaxel loading albumin nanoparticles, *Nanoscale*, 2020, **12**, 16928–16933, DOI: **10.1039/C9NR10941B**.

51 Vikas, A. K. Mehata, M. K. Viswanadh, A. K. Malik, A. Setia, P. Kumari, S. K. Mahto and M. S. Muthu, EGFR Targeted Redox Sensitive Chitosan Nanoparticles of Cabazitaxel: Dual-Targeted Cancer Therapy, Lung Distribution, and Targeting Studies by Photoacoustic and Optical Imaging, *Biomacromolecules*, 2023, **24**, 4989–5003, DOI: **10.1021/acs.biomac.3c00658**.

52 S. E. Park, N. S. El-Sayed, K. Shamloo, S. Lohan, S. Kumar, M. I. Sajid and R. K. Tiwari, Targeted Delivery of Cabazitaxel Using Cyclic Cell-Penetrating Peptide and Biomarkers of Extracellular Matrix for Prostate and Breast Cancer Therapy, *Bioconjugate Chem.*, 2021, **32**, 1898–1914, DOI: **10.1021/acs.bioconjchem.1c00319**.

53 M. Wei, T. Lu, Z. Nong, G. Li, X. Pan, Y. Wei, Y. Yang, N. Wu, J. Huang, M. Pan, X. Li and F. Meng, Reductive response and RGD targeting nano-graphene oxide drug delivery system, *J. Drug Delivery Sci. Technol.*, 2019, **53**, 101202, DOI: **10.1016/j.jddst.2019.101202**.

54 E. Lallana, J. M. Rios De La Rosa, A. Tirella, M. Pelliccia, A. Gennari, I. J. Stratford, S. Puri, M. Ashford and N. Tirelli, Chitosan/Hyaluronic Acid Nanoparticles: Rational Design Revisited for RNA Delivery, *Mol. Pharmaceutics*, 2017, **14**, 2422–2436, DOI: **10.1021/acs.molpharmaceut.7b00320**.

55 S. Fengli, Synthesis method of 3,3′-dithiodipropionic acid bis(N-hydroxyl succinimide ester), CN105315191A, 2016. **https://patents.google.com/patent/CN105315191A/en** (accessed November 26, 2023).

56 S. Maya, L. G. Kumar, B. Sarmento, N. Sanoj Rejinold, D. Menon, S. V. Nair and R. Jayakumar, Cetuximab conjugated O-carboxymethyl chitosan nanoparticles for targeting EGFR overexpressing cancer cells, *Carbohydr. Polym.*, 2013, **93**, 661–669, DOI: **10.1016/j.carbpol.2012.12.032**.

57 S. Zhai, X. Hu, Y. Hu, B. Wu and D. Xing, Visible light-induced crosslinking and physiological stabilization of diselenide-rich nanoparticles for redox-responsive drug release and combination chemotherapy, *Biomaterials*, 2017, **121**, 41–54, DOI: **10.1016/j.biomaterials.2017.01.002**.

58 F. Chen, J. Zhang, L. Wang, Y. Wang and M. Chen, Tumor pHe-triggered charge-reversal and redox-responsive nanoparticles for docetaxel delivery in hepatocellular carcinoma treatment, *Nanoscale*, 2015, **7**, 15763–15779, DOI: **10.1039/C5NR04612B**.

59 S. Yin, J. Huai, X. Chen, Y. Yang, X. Zhang, Y. Gan, G. Wang, X. Gu and J. Li, Intracellular delivery and antitumor effects of a redox-responsive polymeric paclitaxel conjugate based on hyaluronic acid, *Acta Biomater.*, 2015, **26**, 274–285, DOI: **10.1016/j.actbio.2015.08.029**.

60 X. Zhang, Y. Wang, G. Wei, J. Zhao, G. Yang and S. Zhou, Stepwise dual targeting and dual responsive polymer micelles for mitochondrion therapy, *J. Controlled Release*, 2020, **322**, 157–169 **https://www.sciencedirect.com/science/article/pii/S0168365920301632** (accessed November 28, 2023).

61 H. Wang, W. Shi, D. Zeng, Q. Huang, J. Xie, H. Wen, J. Li, X. Yu, L. Qin and Y. Zhou, pH-activated, mitochondria-targeted, and redox-responsive delivery of paclitaxel nanomicelles to overcome drug resistance and suppress metastasis in lung cancer, *J. Nanobiotechnol.*, 2021, **19**, 152, DOI: **10.1186/s12951-021-00895-4**.

62 H. Sun, S. Li, W. Qi, R. Xing, Q. Zou and X. Yan, Stimuli-responsive nanoparticles based on co-assembly of naturally-occurring biomacromolecules for *in vitro* photodynamic therapy, *Colloids Surf., A*, 2018, **538**, 795–801, DOI: 10.1016/j.colsurfa.2017.11.072.

63 K. Vaghasiya, E. Ray, A. Sharma, O. P. Katare and R. K. Verma, Matrix Metalloproteinase-Responsive Mesoporous Silica Nanoparticles Cloaked with Cleavable Protein for "Self-Actuating" On-Demand Controlled Drug Delivery for Cancer Therapy, *ACS Appl. Bio Mater.*, 2020, **3**, 4987–4999, DOI: 10.1021/acsabm.0c00497.

64 P. Patel and J. Shah, Protective effects of hesperidin through attenuation of Ki67 expression against DMBA-induced breast cancer in female rats, *Life Sci.*, 2021, **285**, 119957, DOI: 10.1016/j.lfs.2021.119957.

65 K. Kolanjiappan and S. Manoharan, Chemopreventive efficacy and anti-lipid peroxidative potential of Jasminum grandiflorum Linn. on 7,12-dimethylbenz(a)anthracene-induced rat mammary carcinogenesis, *Fundam. Clin. Pharmacol.*, 2005, **19**, 687–693, DOI: 10.1111/j.1472-8206.2005.00376.x.

66 S. Li, P. E. Saw, C. Lin, Y. Nie, W. Tao, O. C. Farokhzad, L. Zhang and X. Xu, Redox-responsive polyprodrug nanoparticles for targeted siRNA delivery and synergistic liver cancer therapy, *Biomaterials*, 2020, **234**, 119760, DOI: 10.1016/j.biomaterials.2020.119760.

67 Z. Wang, X. Xue, Y. He, Z. Lu, B. Jia, H. Wu, Y. Yuan, Y. Huang, H. Wang, H. Lu, K. S. Lam, T.-Y. Lin and Y. Li, Novel Redox-Responsive Polymeric Magnetosomes with Tunable Magnetic Resonance Property for *In Vivo* Drug Release Visualization and Dual-Modal Cancer Therapy, *Adv. Funct. Mater.*, 2018, **28**, 1802159, DOI: 10.1002/adfm.201802159.

68 K. Xiao, Q. Liu, N. Suby, W. Xiao, R. Agrawal, M. Vu, H. Zhang, Y. Luo, Y. Li and K. S. Lam, LHRH-Targeted Redox-Responsive Crosslinked Micelles Impart Selective Drug Delivery and Effective Chemotherapy in Triple-Negative Breast Cancer, *Adv. Healthcare Mater.*, 2021, **10**, 2001196, DOI: 10.1002/adhm.202001196.

69 R. Wang, H. Yang, A. R. Khan, X. Yang, J. Xu, J. Ji and G. Zhai, Redox-responsive hyaluronic acid-based nanoparticles for targeted photodynamic therapy/chemotherapy against breast cancer, *J. Colloid Interface Sci.*, 2021, **598**, 213–228, DOI: 10.1016/j.jcis.2021.04.056.

70 T. G. Buu, T. T. P. Nhung and N. T. Trang, Characterization of Crilin and Nanocurcumin's Synergistic Effect on Treatment for 7.12-Dimethylbenz[*a*]anthracene (DMBA)-Induced Breast Cancer Mice, *VNU J. Sci.: Med. Pharm. Sci.*, 2018, **34**, DOI: 10.25073/2588-1132/vnumps.4099.

71 V. Akhouri, M. Kumari and A. Kumar, Therapeutic effect of Aegle marmelos fruit extract against DMBA induced breast cancer in rats, *Sci. Rep.*, 2020, **10**, 18016, DOI: 10.1038/s41598-020-72935-2.

72 Y. Guo, M. Chu, S. Tan, S. Zhao, H. Liu, B. O. Otieno, X. Yang, C. Xu and Z. Zhang, Chitosan-g-TPGS Nanoparticles for Anticancer Drug Delivery and Overcoming Multidrug Resistance, *Mol. Pharmaceutics*, 2014, **11**, 59–70, DOI: 10.1021/mp400514t.

73 B. Wei, M. He, X. Cai, X. Hou, Y. Wang, J. Chen, M. Lan, Y. Chen, K. Lou and F. Gao, Vitamin E succinate-grafted-chitosan/chitosan oligosaccharide mixed micelles loaded with C-DMSA for Hg2+ detection and detoxification in rat liver, *Int. J. Nanomed.*, 2019, **14**, 6917, DOI: 10.2147/IJN.S213084.

74 P. Chand, H. Kumar, N. Badduri, N. V. Gupta, V. G. Bettada, S. V. Madhunapantula, S. S. Kesharwani, S. Dey and V. Jain, Design and evaluation of cabazitaxel loaded NLCs against breast cancer cell lines, *Colloids Surf., B*, 2021, **199**, 111535, DOI: 10.1016/j.colsurfb.2020.111535.

75 W. Cabri, D. Ciceri, L. Domenighini, A. Gambini and F. Peterlongo, A crystalline anhydrous form of cabazitaxel, process for the preparation and pharmaceutical compositions thereof, EP3060556A1, 2016. https://patents.google.com/patent/EP3060556A1/en (accessed November 26, 2023).

76 A. K. Jangid, D. Pooja, P. Jain, S. V. K. Rompicharla, S. Ramesan and H. Kulhari, A nanoscale, biocompatible and amphiphilic prodrug of cabazitaxel with improved anticancer efficacy against 3D spheroids of prostate cancer cells, *Mater. Adv.*, 2020, **1**, 738–748, DOI: 10.1039/D0MA00189A.

77 Q. Chen, C. Jia, Y. Xu, Z. Jiang, T. Hu, C. Li and X. Cheng, Dual-pH responsive chitosan nanoparticles for improving *in vivo* drugs delivery and chemoresistance in breast cancer, *Carbohydr. Polym.*, 2022, **290**, 119518, DOI: 10.1016/j.carbpol.2022.119518.

78 U. de J. Martín-Camacho, N. Rodríguez-Barajas, J. A. Sánchez-Burgos and A. Pérez-Larios, Weibull β value for the discernment of drug release mechanism of PLGA particles, *Int. J. Pharm.*, 2023, **640**, 123017, DOI: 10.1016/j.ijpharm.2023.123017.

79 S. Zhang, X. Fan, G. Zhang, W. Wang and L. Yan, Preparation, characterization, and *in vitro* release kinetics of doxorubicin-loaded magnetosomes, *J. Biomater. Appl.*, 2022, **36**, 1469–1483, DOI: 10.1177/08853282211060544.

80 A.-M. Craciun, M. L. Barhalescu, M. Agop and L. Ochiuz, Theoretical Modeling of Long-Time Drug Release from Nitrosalicyl-Imine-Chitosan Hydrogels through Multifractal Logistic Type Laws, *Comput. Math. Methods Med.*, 2019, **2019**, 4091464, DOI: 10.1155/2019/4091464.

81 K. Ghosal, A. Chandra, R. Rajabalaya, S. Chakraborty and A. Nanda, Mathematical modeling of drug release profiles for modified hydrophobic HPMC based gels, *Die Pharmazie-An Int. J. Pharm. Sci.*, 2012, **67**, 147–155 https://www.ingentaconnect.com/content/govi/pharmaz/2012/00000067/00000002/art00009 (accessed February 9, 2024).

82 C. Corsaro, G. Neri, A. M. Mezzasalma and E. Fazio, Weibull Modeling of Controlled Drug Release from Ag-PMA Nanosystems, *Polymers*, 2021, **13**, 2897, DOI: 10.3390/polym13172897.

83 J. B. Minari, G. O. Ogar and A. J. Bello, Antiproliferative potential of aqueous leaf extract of Mucuna pruriens on DMBA-induced breast cancer in female albino rats, *Egypt. J. Med. Hum. Genet.*, 2016, **17**, 331–343, DOI: 10.1016/j.ejmhg.2015.12.008.

84 B. Singh, N. K. Bhat and H. K. Bhat, Partial Inhibition of Estrogen-Induced Mammary Carcinogenesis in Rats by Tamoxifen: Balance between Oxidant Stress and Estrogen Responsiveness, *PLoS One*, 2011, **6**, e25125, DOI: **10.1371/journal.pone.0025125**.

85 W. Wang, D. Luo, J. Chen, J. Chen, Y. Xia, W. Chen and Y. Wang, Amelioration of cyclophosphamide-induced myelosuppression during treatment to rats with breast cancer through low-intensity pulsed ultrasound, *Biosci. Rep.*, 2020, **40**, BSR20201350, DOI: **10.1042/BSR20201350**.